Orographic Cirrus and Its Radiative Forcing in NCAR CAM6

Kai Lyu[1], Xiaohong Liu[1,*], Julio Bacmeister[2], Xi Zhao[1], Lin Lin[1], Yang Shi[1], and Odran Sourdeval[3]

[1]Department of Atmospheric Sciences, Texas A&M University, College Station, TX, USA

[2]Climate and Global Dynamics, National Center for Atmospheric Research, Boulder, CO, USA

[3]Laboratoire d'Optique Atmosphérique, Université de Lille, Villeneuve-d'Ascq, France

Correspondence to: Xiaohong Liu (xiaohong.liu@tamu.edu)

Key points:

- Vertical velocity variance (σ_w) generated by orographic gravity waves (OGWs) is introduced to the cirrus formation in CAM6.
- The sub-grid scale σ_w is increased by OGW-induced fluctuations over mountains in orographic cirrus and agrees better with observations.
- The large σ_w induced by OGWs generates high in-cloud ice number concentrations (> 200 L^{-1}) in orographic cirrus as observed.

This article has been accepted for publication and undergone full peer review but has not been through the copyediting, typesetting, pagination and proofreading process, which may lead to differences between this version and the Version of Record. Please cite this article as doi: 10.1029/2022JD038164.

Abstract

Cirrus clouds play an important role in the Earth's radiative energy budget, thereby affecting the climate state and climate change. Orographic gravity wave (OGW)-induced sub-grid scale vertical velocity (i.e., cooling rate) is not resolved by large-scale models and its impact on ice formation in cirrus clouds is not well quantified. In this study, one sub-grid scale OGW scheme (e.g., McFarlane) is used in the Community Atmosphere Model version 6 (CAM6) to generate vertical velocity variance (σ_w) for cirrus formation. Results from the default model and simulations with the OGW-induced σ_w are evaluated against the DOE ARM Small Particles in Cirrus (SPARTICUS) campaign observations. The OGW based on the McFarlane scheme increases the sub-grid scale σ_w over mountains compared to the default model and improves the model agreement with the SPARTICUS observations. Larger σ_w due to OGWs can trigger more frequent homogeneous nucleation in orographic cirrus and generates a higher number concentration of ice crystals observed during the SPARTICUS campaign. Moreover, our evaluation of the model simulations against satellite observations indicates that the McFarlane scheme generates high in-cloud ice number concentrations (> 200 L^{-1}) in the upper troposphere over mountains and high plateaus at mid- and high-latitudes of the winter hemisphere as shown in the observations. More ice crystals with smaller sizes absorb more infrared radiation (+0.523 ± 0.125 W m^{-2}). The net radiative cloud forcing change at the top of the atmosphere is +0.330 W m^{-2} due to the orographic cirrus.

Keywords: Orographic gravity waves, cirrus, ice nucleation, GCM

Plain Language Summary:

Cirrus clouds occurring frequently in the upper troposphere play an important role in the Earth's radiative budget and the global climate. Large mountains in the globe can produce strong gravity waves propagating upward to the upper troposphere. These orographic gravity waves can induce large vertical velocities and form orographic cirrus which can extend hundreds of miles in the atmosphere. This study introduces orographic gravity waves induced by the mountains to cirrus ice formation in a global climate model, the Community Atmosphere Model version 6 (CAM6). We find that a large amount of ice crystals forms in the simulated cirrus over mountains in the winter hemisphere when orographic gravity waves are included in the cirrus formation. The simulation results are improved when comparing with aircraft and satellite observations. Orographic cirrus induces a warming effect on the global climate.

1 Introduction

Cirrus clouds, covering over 30 % of the Earth's surface, play an essential role in climate (Liou, 1986). Composed of ice crystals, they can reflect solar radiation with a cooling effect, absorb and reemit longwave radiation with a warming effect, and therefore strongly influence the Earth's radiative budgets. The net radiative effect of cirrus clouds and their feedback on global warming is still uncertain (Ceppi et al., 2017; Stephens, 2005; Wetherald and Manabe, 1988). Current global climate models (GCMs) produce a large spread in cirrus feedback, ranging from weakly negative to strongly positive feedback (-0.13 to 1.24 W m^{-2} K^{-1}) (Ceppi et al., 2017).

Vertical velocity is a critical factor in triggering the formation of ice crystals in cirrus clouds. A larger vertical velocity can generate a stronger adiabatic cooling, decrease the parcel's temperature, increase the relative humidity with respect to ice, activate more aerosols, and thus form more ice crystals (Kärcher and Lohmann, 2002). Previous studies show that, when vertical velocity increases from 10 to 100 cm s^{-1}, the number of newly-formed ice particles increases by more than one order of magnitude (Kärcher and Lohmann, 2002). The vertical velocity on smaller scales is more important to the nucleation of ice crystals in cirrus clouds than the synoptic-scale vertical velocity (Mace et al., 2001; Quante and Starr, 2002). In the lower stratosphere and upper troposphere, mesoscale gravity waves are ubiquitous and usually generate strong disturbances (Dinh et al., 2016; Hoyle et al., 2005; Murphy, 2014; Preusse et al., 2014; Shi and Liu, 2016). Orographic gravity waves (OGWs) are one of the most important sources of mesoscale waves (Kärcher and Ström, 2003). In the world, there are a lot of mountains producing OGWs that are observed to generate vertical velocities for the formation of cirrus clouds (Teixeira, 2014; Dean et al., 2007; Dean et al., 2005). Thus, it is necessary for GCMs to represent these orographic cirrus clouds in the models (Dean et al., 2007; Dean et al., 2005).

Many parameterizations of sub-grid scale OGW drag have been developed for GCMs (Alexander and Ortland, 2010; Alpert, 2004; Fritts and Alexander, 2003; Geller et al., 2013; Kim et al., 2003; McFarlane, 1987). The early OGW drag parameterizations were based on the McFarlane theory (McFarlane, 1987), while the improved parameterizations

were further developed based on the anisotropic orography theory (Alpert, 2004; Gregory et al., 1998; Joos et al., 2008; Lott and Miller, 1997; Scinocca and McFarlane, 2000). In addition, a Gaussian distribution was used to characterize the sub-grid scale vertical velocity resulting from gravity waves, with a close fit to the central 68% of the observed vertical velocity spectrum (Bacmeister et al., 1999). However, it may underestimate the probability of vertical velocity of high amplitude (Bacmeister et al., 1999).

Cirrus clouds form through two ice nucleation pathways: homogeneous and heterogeneous ice nucleation (Jensen and Pfister, 2004; Jensen et al., 2010; Jensen et al., 1998; Koop et al., 2000; Liu and Penner, 2005). Homogeneous ice nucleation on aerosol droplet solutions, such as sulfate and nitrate aerosols, requires an ice supersaturation of 40–60 % at temperatures below 235 K. It can generate significant concentrations of ice crystals of about 100–10,000 L^{-1}. Homogeneous nucleation strongly depends on vertical motions (Joos et al., 2008). On the other hand, heterogeneous ice nucleation on ice nucleating particles (INPs) requires a lower ice supersaturation and produces larger-sized ice crystals with lower number concentrations (between 1 and 100 L^{-1}) than homogeneous nucleation. Heterogeneous ice nucleation depends on the efficiency and abundance of INPs such as mineral dust, biological aerosols, black carbon, or other insoluble or partially insoluble particles (Hoose and Möhler, 2012; Murray et al., 2012). The two mechanisms of ice nucleation once occur can compete for water vapor in cirrus clouds (DeMott et al., 2003; Penner et al., 2018; Shi et al., 2017). Ice crystals formed heterogeneously consume water vapor preferentially, and the subsequent homogeneous nucleation can be partially or completely inhibited (DeMott et al., 2003; Eidhammer et al., 2014; Liu et al., 2012; Zhang et al., 2013).

Observational analyses find that the most important dynamic factors for in-situ cirrus formation can be turbulence kinetic energy (TKE) in unstable circumstances and gravity waves in a stable atmosphere (Haag and Kärcher, 2004; Hoyle et al., 2005; Jensen et al., 2010; Jensen et al., 1998; Kärcher and Ström, 2003; Krämer et al., 2016; Krämer et al., 2020). Strictly speaking, gravity waves are essentially a source of TKE when the Richardson number is large in a stable atmosphere. To clearly distinguish TKE from the CLUBB scheme and OGWs from the McFarlane scheme, we exclusively use the term TKE to refer to TKE from CLUBB with a small Richardson number. However, the current version of the Community Atmosphere Model version 6 (CAM6), considers TKE from CLUBB as the only dynamic source for in-situ ice formation. The absence of OGWs in ice nucleation is likely to generate a large bias for ice nucleation over mountains, especially in the winter hemisphere (Barahona and Nenes, 2011; Kärcher and Ström, 2003; Krämer et al., 2016; Krämer et al., 2020; Muhlbauer et al., 2014a). The objective of this study is to calculate the vertical velocity variances from the OGW scheme and to introduce them into the ice nucleation of cirrus in CAM6, with the aim to improve the simulation of orographic cirrus over mountains and high plateaus. The modeled cirrus clouds are evaluated against the in-situ and satellite observations and the radiative forcing of orographic cirrus is estimated.

The remainder of this article is organized as follows. Section 2 describes the model, configuration and parameterizations to represent the σ_w from OGWs. Observational data used in this study are summarized in Section 3. Section 4 compares the model

simulations of cirrus clouds with observational data. The orographic cirrus radiative forcing is also calculated. Summary and conclusions are given in Section 5.

2 Method

2.1 Model description

CAM6, the atmosphere component of CESM2 (Danabasoglu et al., 2020), is used in this study. In CAM6, the Cloud Layers Unified by Binormals (CLUBB) (Golaz et al., 2002a; b) scheme is applied to unify the treatment of the planetary boundary layer, cloud macrophysics, and shallow convection. The two-moment Morrison and Gettelman version 2 (MG2) scheme is applied in CAM6 to treat cloud microphysical processes (Gettelman et al., 2010; Gettelman et al., 2019; Gettelman and Morrison, 2015), which will be discussed more in section 2.2. Aerosol lifecycle and processes are represented by the four-mode version of the Model Aerosol Module (MAM4), which predicts the mass mixing ratios of different aerosol species and number concentrations of aerosol in accumulation, Aitken, coarse and primary carbon modes (Liu et al., 2012; Liu et al., 2016). Deep convection is treated by the Zhang and McFarlane (1995) scheme. The radiative effects of clouds and aerosol are treated by the RRTMG radiation scheme (Iacono et al., 2008).

2.2 MG2 cloud microphysics and ice nucleation

The MG2 microphysics scheme predicts the mass mixing ratios and number concentrations of cloud liquid, cloud ice, rain, and snow, as well as complicated cloud microphysical processes. Aerosol indirect effects are treated including droplet nucleation in warm clouds (Abdul-Razzak and Ghan, 2000) and ice nucleation in stratiform mixed-phase (Wang et al., 2014) and cirrus clouds (Liu and Penner, 2005; Liu et al., 2007). Ice in stratiform cirrus can be formed by in-situ ice nucleation or detrained from convective clouds. The parameterization of in-situ ice nucleation in cirrus clouds considers the homogeneous freezing of sulfate aerosols, heterogeneous nucleation on coarse mode dust, and the competition between the two mechanisms (Liu and Penner, 2005), and the effect of pre-existing ice on ice nucleation (Shi et al., 2015; Shi and Liu, 2016). The nucleated ice number in cirrus is parameterized as a function of sub-grid updraft velocity, temperature, humidity, and sulfate and coarse mode dust number concentrations derived from the detailed parcel model simulations (Liu and Penner, 2005). In the default CAM6, sub-grid vertical velocity variance (σ_w) associated with TKE from CLUBB is used in the ice nucleation parameterization in cirrus clouds.

Sub-grid scale σ_w is an important factor for ice nucleation in cirrus clouds. The CLUBB scheme assumes trivariate probability density functions (PDFs) of vertical velocity, temperature, and total water to calculate the turbulent moments and cloud macrophysical quantities for low-level clouds. However, the multivariate PDF assumptions (with small Richardson numbers) may not represent the dynamics in the upper troposphere. When the atmosphere is stable (with large Richardson numbers), linear gravity waves associated

with steady, unidirectional and stably stratified flows can be generated. The sub-grid scale OGWs based on the theory of linear waves (e.g., the McFarlane scheme) can be applied to describe the dynamics of the upper troposphere, which is currently neglected in TKE from CLUBB.

2.3 Parameterization for σ_w generated from OGWs: the McFarlane scheme

The McFarlane (1987) OGW scheme assumes two-dimensional, steady-state hydrostatic gravity waves and neglects the Coriolis force, which implies the limits imposed on the horizontal wavenumber k on the parameterized OGWs as:

$$\frac{f}{U} \ll k \ll \frac{N}{U}, \tag{1}$$

where f is the Coriolis parameter, U the horizontal wind speed, and N the Brunt-Vaisala frequency.

To excite the OGW drag on the flow, the McFarlane scheme assumes that the stationary OGWs are forced by circularly symmetric orography h with the form as:

$$h = h_m \cos(kx), \tag{2}$$

where h_m is the standard deviation of orography and x is the horizontal dimension positive in the downstream direction. The geographic distribution of standard deviation of orography h_m used in the model is shown in Figure S1. The waves are considered as the linear waves generated when a steady, unidirectional, and stably stratified mean flow blows over the spherical barrier. The wave stress at level n is given as

$$\tau(n) \sim \rho(n)\overline{u'(n)w'(n)}, \quad (3)$$

where $\rho(n)$ is the air density at level n. $\overline{u'(n)}$ is the horizontal average of first-order perturbation of horizontal wind and can be approximated as $\overline{u'(n)} \sim N(n)\delta$. $N(n)$ is the Brunt-Vaisala frequency and δ is the perturbation. $\overline{w'(n)}$ is the horizontal average of first-order perturbation of vertical wind and can be approximated as $\overline{w'(n)} \sim kU(n)\delta$. $U(n)$ is the horizontal wind speed at level n. At the boundary, the wave stress at surface can be calculated as $\tau_{sfc} \sim \frac{1}{L}\int_{-\frac{L}{2}}^{\frac{L}{2}} \rho(0)\overline{u'(0)w'(0)}\, dx$. Here L is the horizontal wavelength. δ is the orographic perturbation and can be approximated as $\delta \sim h$ if no wave dissipation occurs.

In regions where wave dissipation processes can be ignored, the surface OGW stress can be approximated as

$$\tau_{sfc} \approx \frac{kh_m^2}{2}\rho_{sfc}N_{sfc}U_{sfc}, \quad (4)$$

where τ_{sfc} is the excited OGW stress at the surface, N_{sfc} is the Brunt-Vaisala frequency at the surface, U_{sfc} is the horizontal wind speed at the surface, and ρ_{sfc} is the air density at the surface. In the model, the OGW is calculated when $U > 2$ m s^{-1} and $h_m > 5$ m. Otherwise, the surface OGW stress is 0.

Vertical propagation of OGWs is approximated by assuming constant OGW stress up to a saturation level (Lindzen, 1981), where the local wave vertical displacement δ is approximated as $\delta \sim U/N$. At any level n, the vertical displacement and OGW stress is related by

$$\delta^2(n) = \min\left(\frac{|\tau(n)|}{k\rho(n)U(n)N(n)}, \frac{U^2(n)}{N^2(n)}\right). \quad (5)$$

We utilize the OGW stress output from the OGW scheme to calculate δ using Eq. (5). Then, the σ_w of OGWs can be approximated as (Joos et al., 2008; McFarlane, 1987):

$$\sigma_{w,ogw}(\mathrm{n}) \sim kU(n)\delta(n). \quad (6)$$

To calculate the wavenumber *k* at level n, the wavelength *L* (=$2\pi/k$) of sub-grid scale OGWs in the calculated layer is set to 10 km. *L* is considerably shorter than the length scales of OGWs cited in previous descriptions of the McFarlane scheme in CAM6, however, in practice this is poorly constrained quantity and we regard it as a tuneable parameter (from 10 to 100 km). A shorter wavelength *L* of OGWs may induce a stronger σ_w for ice formation at level *n*. The OGW-induced sub-grid scale $\sigma_{w,ogw}$ is introduced to calculate the total sub-grid scale σ_w:

$$\sigma_w^2(\mathrm{n}) = \sigma_{w,tke}^2(\mathrm{n}) + \sigma_{w,ogw}^2(\mathrm{n}) \,, \quad (7)$$

The σ_w from the sub-grid scale turbulence motion, $\sigma_{w,tke}(n)$, is calculated from TKE in CLUBB as in the default model (Eq. 6 in Gettelman et al., 2010). The new $\sigma_w(n)$ which includes both TKE from CLUBB and sub-grid scale OGWs from McFarlane, is applied to the ice nucleation parameterization (Liu and Penner, 2005; Liu et al., 2007).

There may be an argument that an intersection may occur between TKE from CLUBB and sub-grid scale OGWs from the McFarlane scheme. Although in the stable atmosphere the regimes from turbulence and gravity waves appear continuum, turbulence (with small Richardson numbers) and OGWs (with large Richardson numbers) are parameterized separately in the model. CLUBB does not consider the sub-grid scale

orography in its parameterization and thus TKE from CLUBB may not account for the contribution from sub-scale OGWs. In addition, our following analysis (in section 4.1) shows that $\sigma_{w,tke}(n)$ from CLUBB can only generate very small σ_w (about 0.001 m s^{-1}) over mountains, while the aircraft can observe much higher σ_w in orographic cirrus. As a result, the intersection between TKE from the CLUBB scheme and OGWs from the McFarlane scheme is quite unlikely.

2.4 Model experiments

The horizontal resolution used in CAM6 is $0.9^o \times 1.25^o$ with 56 vertical layers. Model experiments with the default CAM6 and CAM6 with the aforementioned the OGW scheme (i.e., the McFarlane scheme) are conducted from January 2009 to June 2010, with the first year used for model spinning up. Additionally, two sensitivity experiments with the McFarlane scheme but turning off either homogeneous or heterogeneous ice nucleation are conducted. In all these experiments, modeled horizontal wind components (U and V) are nudged toward the MERRA-2 reanalysis data with a relaxation time of 6 hours. The model results are output instantaneously every 10 s along the flight tracks during the Small Particles in Cirrus (SPARTICUS) campaign supported by the Department of Energy (DOE) Atmospheric Radiation Measurement (ARM) program. When the aircraft flies within the same model grid box, the model outputs the same values within one model time step (30 mins). High-frequency model outputs along the flight track can be redundant. However, since the aircraft may fly into multiple grid boxes within one model time step, it is not recommended to set the time interval for model output too long.

For comparison with the liDAR-raDAR (DARDAR) satellite observations (Delanoë and Hogan, 2010), we conduct nudged model experiments with the default CAM6 and CAM6 with the McFarlane scheme from October 2006 to December 2009, with the first three months used for model spinning up. Finally, we conduct 6-year free-running model simulations with the default CAM6 and CAM6 with the McFarlane scheme forced by prescribed present-day climatological sea surface temperatures and sea ice extent to estimate the OGW-generated cirrus radiative forcing. A list of all model experiments used in this study is given in Table 1.

3 Observational Data

3.1 SPARTICUS observations

The data obtained during the SPARTICUS field campaign are used in this study. The campaign took place from January to June in 2010 over mountains in the Central United States, and its flight tracks are shown in Fig. 1. There are about 150 hours of research flights targeting at cirrus clouds. Temperature is measured by the Rosemount probe Model 102 with a precision of ±0.5 ℃. Vertical velocity of air motions is measured by the Aircraft-Integrated Meteorological Measurement System-20 (AIMMS-20) instrument carried by Learjet 25 (Muhlbauer et al., 2014b). The absolute accuracy of vertical velocity measurements is 0.75 m s^{-1}. Although the absolute accuracy of the instrument is too large to measure the vertical velocity, σ_w can be used to represent the perturbation as a reasonably accurate measure (Lenschow, 1972; Muhlbauer et al., 2014b). In order to

investigate the OGW effects in ice nucleation, this study focuses on the high σ_w in cirrus clouds. Previous studies indicated that 0.1 m s^{-1} is a reasonable indicator to categorize the high σ_w in cirrus clouds (Krämer et al., 2016; Krämer et al., 2020). Thus, 0.1 m s^{-1} threshold is applied in our analysis to show the impact of OGWs on modeled vertical velocity variance. Ice particles are measured by the two-dimensional stereo-imaging probes (2D-S) for a size range of 10–3000 μm. The bias on the number concentration of small-sized ice crystals is minimized because the ice shattering effect is addressed on the 2D-S probe (Lawson, 2011). The observational data are available at a frequency of 1 Hz. Considering the speed of the aircraft (~230 m s^{-1}), 430 s of the flight is about 100 km, which is the length of the model's horizontal resolution (1 degree). Therefore, we use a running average of 430 s measurement data to compare with the model results (Patnaude et al., 2021).

3.2 DARDAR data

DARDAR-Nice data from 2007 to 2009 are used to evaluate the simulated ice number concentration (Sourdeval et al., 2018). DARDAR-Nice product is developed based on a synergetic ice cloud retrieval algorithm (VarCloud algorithm) (Delanoë and Hogan, 2010) combining the CloudSat and the Cloud-Aerosol Lidar and Infrared Pathfinder Satellite Observation (CALIPSO). Ice number concentrations are provided along the CloudSat tracks (1.7 km) with a vertical resolution of 60 m. Three size thresholds are set for ice number concentrations contained in the retrieved data, which are 5, 25 and 100 μm. Ice number concentrations with a minimum size of 5 μm are used in this study because the number concentrations of small ice particles are essential when studying ice

nucleation in cirrus clouds. To compare with the DARDAR data, we derive the N_i with ice crystal diameter larger than 5 μm from the total N_i in clouds with IWC $\geq 1 \times 10^{-3}$ g kg^{-1} and grid-averaged ice cloud fraction larger than 0.01 from simulation results (Eidhammer et al., 2014). The model results are outputted along satellite tracks to facilitate the comparison.

4 Results

4.1 Model comparison with SPARTICUS observations

First, we categorize cirrus clouds before studying the effects of OGWs on ice nucleation. In this study, we discuss two categories of cirrus that can be simulated in CAM6. The first category of cirrus is ridge-crest cirrus (Muhlbauer et al., 2014a) and belongs to in-situ origin cirrus (Krämer et al., 2016), which includes orographic cirrus incited by OGWs. The second category of cirrus includes liquid origin cirrus (Krämer et al., 2016), which is detrained from convective clouds, and in-situ origin cirrus predominated by TKE from CLUBB. Other categories of cirrus, such as jet stream cirrus, will not be discussed in this study.

Muhlbauer et al. (2014a) summarized the number of flights, number of days, and list of days for SPARTICUS observations according to cirrus categories and atmospheric states. There were 10 flights in five days (March 19, 30, April 1, 28, and 29) downstream of the mountains and ridge-crest cirrus was observed. Table 2 summarizes the range of meteorological conditions and ice microphysical properties for cirrus clouds and ridge-

crest cirrus in the SPARTICUS observations and CAM simulations. In SPARTICUS, measured cirrus clouds are defined as clouds at $T \leq$ -40 ℃ with in-cloud ice number concentration (N_i) ≥ 0.01 L^{-1}. In model simulations, cirrus clouds are defined as clouds at $T \leq$ -40 ℃ with $N_i \geq 0.01$ L^{-1} and ice water content (IWC) $\geq 1 \times 10^{-5}$ g m^{-3}. In addition, we apply the size cut method of Eidhammer et al. (2014) to derive the properties (such as N_i, IWC and diameters) for those ice crystals with diameters ≥ 10 μm from the CAM6 results, consistent with the measurements by the 2D-S probe (Section 3.1). Because observations do not distinguish snow from cloud ice, the modeled cloud ice and snow are combined to derive the grid mean quantities (N_i, IWC and diameters) to compare with observations.

4.1.1 Vertical velocity and potential temperature variances

Figure 2 shows the annual mean σ_w at 250 hPa from the CAM simulations. The global annual mean σ_w in the CTL experiment is 0.046 m s^{-1}, with the maximum σ_w at 0.27 m s^{-1} over the tropical regions. Over the mountain regions, high σ_w values can hardly be generated. In the McFarlane experiment, we can see a completely different global distribution of sub-grid scale σ_w. There are high σ_w values ≥ 0.25 m s^{-1} over the mountainous regions, such as the Himalayas, the Rocky Mountains, the Andes Mountains, the Antarctic peninsula, Greenland, and the Alps, which are induced by OGWs. In addition, our results are consistent with the previous studies that similar large σ_w values are found in the tropics and over mountains in the upper troposphere (Barahona et al., 2017; Barahona and Nenes, 2011; Joos et al., 2009; Joos et al., 2008; Krämer et al., 2016; McFarlane, 1987).

Figure 3 shows the annual zonal mean σ_w in different simulations. In the CTL experiment, large σ_w values (≥ 0.1 m s^{-1}) are found only in the tropical regions owing to the contribution of TKE from CLUBB. There are hardly high σ_w values at the mid- and high-latitudes associated with mountains because the contribution from gravity waves is not accounted for. When we introduce σ_w induced by sub-grid scale OGWs, high σ_w values (≥ 0.1 m s^{-1}) are now simulated around the 30–70^o N, 5^o N and 80–90^o S (Antarctic regions) in the McFarlane experiment. The high mountains primarily located in the mid- and high-latitudes contribute to the significant increases in σ_w. The McFarlane scheme thus leads to a different distribution of zonal mean σ_w which captures the high values (≥ 0.1 m s^{-1}) often observed over mountains.

The probability density functions (PDFs) of σ_w along the flight trajectories during the SPARTICUS campaign are shown in Figure S2. The PDFs of σ_w values in the McFarlane experiment exhibit longer tails than in the CTL experiment indicating that the maximum σ_w values increase when adding OGW-induced σ_w (Fig. S2a, Fig. S2b, and Fig. S2c). In ridge-crest cirrus, the fast-speed σ_w simulated in the McFarlane experiment shows a better agreement with the observation since the CTL experiment only simulates two fast-speed occurrences.

Table 3 shows the occurrence of the fast-speed σ_w in cirrus clouds and ridge-crest cirrus along SPARTICUS flight tracks from observations and simulations. For cirrus, the fast-speed σ_w occurrence in the McFarlane experiment increases significantly compared with the CTL experiment and matches well with the observation. Thus, OGWs contribute a

new source of sub-grid scale σ_w, which increases the simulated σ_w in both maximum values and the occurrence of fast-speed σ_w, in better agreement with the observations. The discrepancy of the fast-speed σ_w occurrence between the McFarlane experiment and the observation in ridge-crest cirrus can be explained by a lack of other possible dynamic sources such as small-scale OGWs (L < 10 km) and a lack of horizontal propagation of gravity waves in the model (Haag and Kärcher, 2004; Jensen et al., 2010; Joos et al., 2008; Kärcher and Ström, 2003).

Finally, although the occurrences of cirrus and ridge-crest cirrus with fast-speed σ_w increase significantly with the OGW-induced σ_w (Table 3), the occurrences of cirrus and ridge-crest cirrus in the McFarlane experiment increase slightly, compared with the CTL experiment (Table 2). This result indicates that the CTL experiment can simulate the occurrences of cirrus and ridge-crest cirrus but tends to underestimate σ_w. The McFarlane experiment can significantly reduce the underestimation of σ_w with the contribution from OGWs.

There are a total of 53987 samples during the SPARTICUS campaign. After quality controls, 15168 samples are available for observed vertical velocity variance. To better illustrate the effects of OGW-induced fluctuations, we also use the potential temperature variance (θ'^2) to represent the sub-grid scale fluctuation. The θ'^2 is extracted from flight tracks when the aircraft flew above 400 hPa. Also, the data collected during the aircraft's taking off and landing are excluded. The potential temperature fluctuation θ' at time t along aircraft flights is calculated by the following equation,

$$\theta'(t) = \theta(t) - \bar{\theta} \quad (8)$$

where $\bar{\theta}$ is obtained by averaging θ every 430 s, and $\theta(t)$ is the instantaneous potential temperature at time *t*. About 42 % of available data of θ'^2 is derived in selected segments during the entire SPARTICUS campaign.

From the model simulations, we obtain θ' as follows,

$$\theta' = -\delta(z)\frac{\partial\theta}{\partial z} = \rho g \delta(z)\frac{\partial\theta}{\partial p}. \quad (9)$$

Figure S3 compares the PDFs of the sub-grid scale potential temperature variance θ'^2 between the observations and simulations. On all tracks, the PDF of θ'^2 exhibits higher probabilities of high θ'^2 in the McFarlane experiment than that in the default model experiment (Fig. S3a). It indicates that with OGW-induced fluctuations, the simulated sub-grid scale fluctuation θ'^2 increases, and its PDF matches better with the observation. The θ'^2 PDF in the McFarlane experiment is more similar to the observation over mountains (Fig. S3b). It is because that since OGWs are induced by the high mountains, its effect on θ'^2 is more significant over mountains. However, the discrepancy in θ'^2 between the observation and the McFarlane experiment still exists, indicating a lack of other possible sources that can produce high θ'^2 in the model (Krämer et al., 2016; Richter et al., 2010).

Figure 4 compares the fast-speed σ_w in ridge-crest cirrus between model simulations and observations along the SPARTICUS flight tracks. The σ_w values in the CTL experiment are usually very small (~0.001 m s^{-1}) with the contribution solely from TKE from CLUBB (Fig. 4a). The large $\sigma_w \geq 0.1$ m s^{-1} over mountains due to OGWs cannot be

reproduced accurately if only the contribution of TKE from CLUBB is considered. By adding the contribution from OGWs, large σ_w values are generated in the McFarlane (Fig. 4b), McFarlane-Hete (Fig. 4d) and McFarlane Homo (Fig. 4c) experiments. The median values of simulated σ_w in the McFarlane experiment range from 0.11 to 0.32 m s^{-1} and can reach to 0.7 m s^{-1}. With large σ_w values, the fast-speed σ_w in simulations with the McFarlane parameterization shows a better agreement with the observation in orographic cirrus.

4.1.2 In-cloud ice number concentration

Figure 5 shows a comparison of modeled N_i with SPARTICUS observations as a relationship with temperature in ridge-crest cirrus. The median values of observed N_i range from 31 to 184 L^{-1} at temperatures above 220 K and increase to about 1000 L^{-1} when temperature approaches 210 K. This is consistent with the trend that homogeneous nucleation tends to occur at lower temperature (Liu and Penner, 2005; Liu et al., 2007). The simulated N_i in the CTL experiment (Fig. 5a) is much lower compared with the observations, the median values of which range from 2.2 L^{-1} to 38.0 L^{-1}. The reason can be explained that the CTL experiment cannot reproduce the sub-grid scale σ_w ($\geq$ 0.1 m s^{-1}) accurately without the contribution of the OGWs (Fig. 5a). The small sub-grid scale σ_w is not able to activate homogeneous nucleation and thus generates a low concentration of ice crystals via heterogeneous nucleation (Fig. 5a and Fig. 5d). We note that some simulated N_i values in the CTL experiment (Fig. 5a) can reach up to 200 L^{-1} at 215 K. The detailed analysis suggests that they may be from some cirrus other than orographic cirrus. The high values are simulated when the aircraft has just taken off or is about to land. The simulated high N_i is not formed in-situ and may be not from orographic cirrus.

They are pre-existing ice crystals that are generated in previous time steps in other grids and transported to the target grids by advection or sedimentation. The majority of data in those five days are representative to show the characteristics of orographic cirrus. However, it is inevitable that some ice crystals may be produced from other sources (e.g., convection detrainment) in those five days.

In comparison, the median N_i in the McFarlane experiment ranges from 30.3 L^{-1} to 457.4 L^{-1} (Fig. 5b) and matches well with the McFarlane-Homo experiment (Fig. 5c) and the observation. By employing the OGW-induced fluctuations in simulated orographic cirrus, sub-grid scale σ_w is increased. The larger sub-grid scale σ_w enhances the occurrence of the homogeneous nucleation in orographic cirrus and produces higher N_i in the McFarlane experiment. Homogeneous nucleation becomes the dominant ice nucleation mechanism of ridge-crest cirrus in the McFarlane experiment, just as observed in the SPARTICUS campaign.

4.1.3 Ice water content

Figure 6 compares the IWC as a function of temperature between observations and simulations in ridge-crest cirrus. The simulated IWCs in all simulations are underestimated compared with observations. The median IWC in the CTL experiment is from 8.4×10^{-5} g m^{-3} to 0.004 g m^{-3} (Fig. 6a). The median IWCs in the McFarlane experiment are larger, ranging from 4.0×10^{-4} g m^{-3} to 0.01 g m^{-3} (Fig. 6b). With OGW-induced σ_w, simulated IWC increases. Most of the simulated ice mass in CAM6 are contributed from the vapor depositional and accretional growth of ice crystals produced

from ice nucleation (Gettelman et al., 2010). With OGW-induced σ_w, σ_w is large enough to trigger the homogeneous nucleation. Smaller ice crystals from homogeneous nucleation sediment more slowly and autoconvert less, hence decreasing the sink of ice and leading to the increase of IWC. In addition, more new ice may also provide surface areas for ice depositional growth. As a result, IWC in the McFarlane experiment increases and helps to fix the underestimation of IWC, in a better agreement with observations.

4.1.4 Ice number-weighted mean diameter

The comparison of simulated ice number-weighted mean diameter (D_i) with observations in ridge-crest cirrus is shown in Fig. 7. D_i in the CTL experiment (Fig. 7a) ranges from 26.7 to 114.9 μm. D_i in the McFarlane experiment (Fig. 7b) is much smaller, between 20.9 and 71.6 μm, similar to the McFarlane-Homo experiment (Fig. 7c) and the observation. With σ_w contributed from OGWs, D_i decreases significantly. In the CTL experiment, heterogeneous nucleation generates large-size ice crystals as indicated by the similar D_i between the CTL and McFarlane-Hete experiments (Fig. 7a and Fig 7d). However, in the McFarlane experiment, homogeneous nucleation triggered by the larger σ_w generates more ice crystals with a smaller size compared to the CTL experiment, in much better agreement with the observation.

4.1.5 Case studies

To further investigate the effects of OGWs on cirrus, case studies are conducted. We examine the meteorology associated with each flight track and compare the σ_w and N_i in both simulations and observations. Two cases are selected. The first case, which occurred

on April 11, 2010, involves orographic cirrus. The second case, which took place on June 14, 2010, involves cirrus clouds resulting from convective detrainment and turbulence. Their flight tracks are shown in Fig. S4.

On April 11, 2010, the aircraft was flying on the 200 hPa ridge and above the Rocky Mountains. The stable atmospheric layers and high mountains provide ideal conditions to form orographic cirrus. During the flight, some σ_w values > 0.7 m s^{-1} were observed over the mountains with a large standard deviation of orography (~500 m) (Fig. 8a). In the CTL experiment, the simulated σ_w is contributed by TKE from CLUBB only and the model does not generate as many large σ_w > 0.1 m s^{-1} as observed. As a result, the CTL experiment is not able to activate as many ice crystals as observed. However, the McFarlane experiment successfully simulates the observed large σ_w. The large sub-grid scale σ_w is dominated by the OGW component of σ_w over high mountains (Fig. 8a), which triggers the homogeneous nucleation and forms the high concentrations (200–359 L^{-1}) of ice crystals at cold temperatures (< 235 K) (Fig. 8b).

On June 14, 2010, the aircraft was flying on the east of the trough at 200 hPa and the northwest edge of the low-pressure system at 800 hPa. The atmospheric layers were unstable with some developing convective systems. The observed cirrus clouds were confirmed as anvils (Muhlbauer et al., 2014a), which indicates that a large number of ice crystals (10^4–10^5 L^{-1}) are detrained from convective clouds. Detrainment can bring a large number of ice crystals from convective clouds to stratiform cirrus clouds. The sudden surges of N_i in simulations between 21:15 and 21:30 UTC are caused by detrained ice

from convective clouds because heterogeneous nucleation cannot generate very high N_i ($> 10^4$ L^{-1}), and homogeneous nucleation does not occur at temperatures larger than 235 K (Fig. 9b). Fig. 9a also shows that between 21:35 and 22:05 UTC in the CTL and McFarlane experiments, there are large σ_w (> 0.1 m s^{-1}) contributed by TKE from CLUBB. Large σ_w due to TKE from CLUBB can generate high active ice nucleation particles and tend to generate high N_i in those regions. On the contrary, σ_w induced by OGWs has little contribution to the large σ_w and hardly has any direct effects on N_i. In short, OGWs had little direct impact on ice nucleation in the cirrus on June 14.

4.2 Model comparison with DARDAR

Next, we compare the model simulations with satellite retrievals to examine the global impacts of OGWs on cirrus microphysical properties.

Figure 10 shows the global N_i at 226 hPa from the DARDAR data and model simulations in boreal summer (June, July, August (JJA)) and winter (December, January, and February (DJF)). In the CTL_D experiment, the simulated N_i compares poorly with observations (Fig. 10c and Fig. 10d). In the McFarlane_D experiment, the simulated N_i in the winter seasons for regions over mountains matches well with observations. The simulated high N_i (> 200 L^{-1}) values are over the Andes Mountains and the Antarctic high plateau in JJA (Fig. 10e and Fig. 10g) and over the Tibet Plateau, the Rocky Mountains, Greenland and the Alps Mountains in DJF (Fig. 10f and Fig. 10h). From the discussions in the above sections, the mountains and high plateaus can enlarge the sub-grid scale σ_w and increase the occurrence of homogeneous nucleation in cirrus clouds. The CTL_D

experiment is not able to activate sufficient aerosols for ice nucleation with σ_w only from TKE from CLUBB over high latitudes in the winter hemisphere. The introduction of σ_w due to OGWs significantly improves the simulation of N_i compared with the observation. In addition, there are more mountains and high plateaus in the Northern Hemisphere than in the Southern Hemisphere. OGWs play a more important role in the winter hemisphere when the atmosphere is more stable. In the summer hemisphere, anvils prevail other types of cirrus and the dominant source of ice crystals in anvils is convective detrainment. As a result, the increase of global mean N_i is more significant in DJF (10.52 L^{-1} in Fig. 10h) than in JJA (8.66 L^{-1} in Fig 10g). However, there are still large discrepancies of high N_i (> 200 L^{-1}) over oceans. It indicates that other sub-grid scale fluctuation sources are not considered for ice nucleation or convection does not detrain enough ice in the model, which is more likely over the ocean.

In the upper troposphere of the summer hemisphere, due to the presence of large TKE-induced σ_w and strong detrainment, OGW-induced σ_w is usually too small to influence N_i. However, over the Southern Andes Mountains and in the Antarctic peninsula in austral summer, orographic cirrus is important and generates a high number concentration (> 200 L^{-1}) of ice crystals (Fig. 10h). The possible reason is that convective detrainment and TKE from CLUBB does not generate many cirrus clouds in summer over those regions, as seen in the CTL_D experiment (Fig. 10d). As one of the world's highest mountains, the Andes Mountains can induce large σ_w (> 0.1 m s^{-1}) in the upper troposphere. The larger σ_w may increase the occurrence of homogeneous nucleation in the McFarlane_D experiment. Many more aerosols can be thus activated to form a larger number of ice

crystals in summer. In addition, Mitchell and Garnier et al. (2018) found that the ice number concentrations in high-latitude cirrus tend to be higher than those in tropical cirrus based on the CALIPSO data analysis. With OGWs, N_i in cirrus appears to be higher in the high latitudes than in the tropical regions, as shown in Fig. 10e and Fig. 10f.

Figure 11 compares the zonal mean N_i between DARDAR and simulations in JJA and DJF. The maximum N_i centers appear in the winter hemisphere in the upper troposphere (Fig. 11a and Fig. 11b). These centers are in mid- and high-latitudes over the mountains and high plateaus. The mountains and high plateaus can induce significant sub-grid scale fluctuations and activate more aerosols to increase the N_i in the McFarlane_D experiment than the CTL_D experiment.

However, there are still some discrepancies in N_i between the McFarlane_D experiment and the observations in the upper troposphere. The discrepancies can be caused by a lack of sub-grid scale fluctuations induced by other gravity waves (Kärcher et al., 2019; Plougonven and Zhang, 2014; Prasad et al., 2019) or by bias in simulated aerosol properties (Shan et al., 2021; Shi and Liu, 2019; Wu et al., 2020; Yu et al., 2019) and deficiency in ice nucleation parameterizations (Shi and Liu, 2016). The abnormal simulated high-N_i values in the lower stratosphere are all sporadic cases and have little effect on cloud bulk properties and climate forcing.

4.3 Climate forcing of orographic cirrus

In order to investigate the impacts of orographic cirrus on global cloud properties and radiative forcing, we conducted free-running simulations using CAM6 (Table 1). As shown in Fig. 12a, grid-averaged ice number concentration (AWNI) increases over the mountain areas in the McFarlane-Climo experiment from 1 to 166 L^{-1}, compared with the CTL-Climo experiment. Grid-averaged IWC increases from 0.1 to 0.55 mg m^{-3} over high mountains in high latitudes, such as the Northern Rocky Mountains, Greenland, the Southern Andes Mountains and the Antarctic continents (Fig. 12b).

Over the Northern Rocky Mountains, the Southern Andes Mountains, and the Antarctic Peninsula, grid-averaged ice effective radius (AREI) decreases (Fig. 12c) and AWNI increases by one order of magnitude (Fig. 12a). It indicates that more ice crystals with smaller sizes are generated with large sub-grid scale σ_w (> 0.1 m s^{-1} in Fig. S5a) excited by these high mountains. We can infer that in these regions, the larger sub-grid scale σ_w due to OGWs increases the occurrence of homogeneous nucleation in orographic cirrus. Sulfate aerosols are activated to form cirrus with higher N_i and smaller sizes compared to the CTL-Climo experiment.

On the other hand, over the Himalayas, AWNI increases from 1 to 10 L^{-1} (Fig. 12a) while AREI does not change much (Fig. 12c). In this region, the INP (coarse mode dust) number concentration has a high value, reaching over 12 L^{-1} (Fig. S5b) due to the deserts. Because heterogeneous nucleation requires nucleation sites on INP that reduce the free energy barrier and homogeneous nucleation does not, dusts via heterogeneous nucleation

are activated before homogeneous nucleation (Liu, 2000). INP can deplete the supersaturation and thus inhibit the occurrence of homogeneous nucleation. The large σ_w activates INPs and generates more ice crystals (1–10 L^{-1}) via the heterogeneous nucleation compared to the CTL-Climo experiment.

Ice crystals in orographic cirrus absorb more longwave radiation emitted from the surface and have a more positive longwave cloud forcing (LWCF). At the top of the atmosphere (TOA), the LWCF of orographic cirrus calculated as the difference of LWCF between the McFarlane-Climo experiment and the CTL-Climo experiment is +0.523 ± 0.125 W m^{-2} on the annual global mean (Fig. 12d). The LWCF from the McFarlane-Climo experiment is 24.3 W m^{-2}, closer to the observed LWCF of 26.1 W m^{-2} from CERES-EBAF (Cloud and the Earth's Radiant Energy System Energy Balanced and Filled) (Loeb et al., 2009; Zhao et al.,2017), compared to 23.7 W m^{-2} from the CTL-Climo experiment (Table S1). Since the extinction coefficient of ice crystals in shortwave depends on many factors such as shape, size, and number concentration of ice crystals and the incident angles, the change of shortwave cloud forcing (SWCF) is more complicated. At the TOA, the mean SWCF is -0.192 ± 0.362 W m^{-2} (Fig. 12e), and the net cloud forcing (NetCF) is +0.330 ± 0.457 W m^{-2} (Fig. 12f). Thus, with OGW-induced σ_w, orographic cirrus leads to a positive net cloud forcing. The positive cloud forcing occurs mostly over mountains in winter hemispheres. The global average changes of high cloud fraction (Fig. 12g) and total cloud fraction (Fig. 12h) are very small.

5 Summary and Conclusions

In this study, we introduce the sub-grid scale σ_w, derived from the McFarlane generated OGWs, to investigate its impact on cirrus ice nucleation in CAM6. We compare the simulation results with aircraft and satellite data to evaluate the modeled microphysical properties of cirrus clouds. Climatological simulations are also conducted to investigate the effects of OGW-induced σ_w on the cloud properties and radiative forcing.

Observational data from the SPARTICUS campaign are used to evaluate the simulated microphysics of cirrus clouds. OGWs in the McFarlane experiment generate larger sub-grid scale σ_w over mountainous regions and show a better agreement with observations. In the CTL experiment, too small σ_w induced only by TKE from CLUBB compared to the observation leads to the low bias of ice crystal number concentrations in orographic cirrus via heterogeneous nucleation. In the McFarlane experiment, larger σ_w induced by OGWs enhances the occurrence homogeneous nucleation and changes the dominant ice nucleation mechanism in orographic cirrus to be homogeneous nucleation. The model is able to match observed ice number concentration and number-weighted mean radii of orographic cirrus. The model also improves the simulation of IWC in the McFarlane experiment. One case study of orographic cirrus confirms that the larger σ_w induced by OGWs generates much higher N_i via homogeneous nucleation in orographic cirrus compared to the CTL experiment.

The DARDAR retrieved data from 2007 to 2009 are used to assess the simulation results on the global scale. With the sub-grid scale σ_w induced by OGWs, the McFarlane scheme

leads to an improved global distribution of N_i which captures the high N_i often observed over mountains, especially in the winter hemisphere. Orographic cirrus may be important over the Southern Andes Mountains and the Antarctic peninsula in austral summer. More high-N_i centers can be simulated in high latitudes than in tropical regions, as observed in previous studies (Mitchell et al., 2018).

Climatological simulations are conducted to study the impact of sub-grid scale σ_w induced by OGWs on cloud properties and radiative forcing through ice nucleation. Sub-grid scale σ_w increases grid-averaged ice number concentrations significantly by one or two orders of magnitude over mountains and high plateaus. Grid-averaged IWC increases on the order of 0.1 mg m^{-3} over high mountains in high latitudes. Grid-averaged ice effective radius decreases over the Northern Rocky Mountains, the Southern Andes Mountains, and the Antarctic Peninsula. Over the Himalayas, grid-averaged ice effective radius does not change much. Orographic cirrus leads to a net positive radiative forcing of $+0.330 \pm 0.457$ W m^{-2} at the TOA and reduces the LWCF bias in CAM6 compared to the observation. The occurrence of orographic cirrus with high ice number concentrations may also influence the cirrus feedback predicted by CAM6, to be further quantified in the future study.

The McFarlane OGW scheme performs well in generating sub-grid scale fluctuations for ice nucleation. In future studies, the more complicated OGW schemes, which consider the anisotrophic orography and low-level blocking, such as the ridge-β scheme and the ridge-ϒ scheme, can be used to further improve the simulation of OGWs. For cloud

dynamics driving the ice nucleation, other sub-grid scale σ_w sources should be considered in addition to OGWs, such as non-orographic gravity waves. Reducing the bias in simulated aerosols (e.g., INPs) can further improve the simulation of ice number concentration in the upper troposphere. Last, it is important to increase the horizontal and vertical resolution in GCMs in the upper troposphere and lower stratosphere to better simulate cirrus.

Our work shows clearly that the CLUBB scheme in CESM2 cannot represent the dynamics of the upper troposphere. Turbulence from CLUBB is not able to reproduce the observed sub-grid scale σ_w in the upper troposphere which is important for ice nucleation in cirrus clouds. As a result, CESM2 underestimates substantially N_i hence biasing the properties of cirrus and by extension the radiative balance of the Earth. The low bias of N_i found in this study can be an important factor for the too low LWCF in CESM2. Since CESM2 is a major model participating in the climate assessments our results of CESM2 biases in the properties and radiative effects of cirrus imply further uncertainty in the climate predictions by CESM2. Future CESM2 developments should make an effort to reduce the biases in cirrus properties (e.g., N_i) by introducing the sub-grid scale σ_w from gravity waves to the model cloud microphysical parameterization.

Acknowledgements

Xiaohong Liu and Kai Lyu acknowledge funding support from US National Science Foundation (grant No. AGS-1642289/2001903). The authors would like to acknowledge the use of computational resources (https://doi.org/10.5065/D6RX99HX) at the NCAR-

Wyoming Supercomputing Center provided by the National Science Foundation and the State of Wyoming and supported by NCAR's Computational and Information Systems Laboratory. We acknowledge Patnaude Ryan, Minghui Diao, Suqian Chu, Xiangjun Shi, and Chenglai Wu for their help in dealing with observational data. We also thank Mingxuan Wu and Meng Zhang for their help in dealing with simulation data.

Data availability Statement

The Community Earth System Model version 2.1.0 (CESM2.1.0) is available at Downloading CESM2 (CESM2.1) — CESM CESM2.1 documentation (escomp.github.io) . The model datasets are archived at https://doi.org/10.5281/zenodo.7734751. Data used for this work was obtained during the SPartICus field campaign. These data are freely available to interested researchers through the DOE ARM program. Data from the 2D-S and other cloud probes can be accessed (http://campaign.arm.gov/sparticus/measurements). The DARDAR-Nice data is provided by the AERIS/ICARE data center (https://www.icare.univ-lille.fr/dardar/data-access/).

References

Abdul-Razzak, H., and S. J. Ghan (2000), A parameterization of aerosol activation: 2. Multiple aerosol types, Journal of Geophysical Research: Atmospheres, 105(D5), 6837-6844, doi:https://doi.org/10.1029/1999JD901161.

Alexander, M. J., and D. A. Ortland (2010), Equatorial waves in High Resolution Dynamics Limb Sounder (HIRDLS) data, Journal of Geophysical Research: Atmospheres, 115(D24), doi:https://doi.org/10.1029/2010JD014782.

Alpert, J. (2004), Sub-grid scale mountain blocking at NCEP, paper presented at Proc. of 20th Conf. on Weather and Forecasting, Seattle, WA, USA.

Bacmeister, J. T., S. D. Eckermann, A. Tsias, K. S. Carslaw, and T. Peter (1999), Mesoscale Temperature Fluctuations Induced by a Spectrum of Gravity Waves: A Comparison of Parameterizations and Their Impact on Stratospheric Microphysics, Journal of the Atmospheric Sciences, 56(12), 1913-1924, doi:https://doi.org/10.1175/1520-0469(1999)056<1913:Mtfiba>2.0.Co;2.

Barahona, D., A. Molod, and H. Kalesse (2017), Direct estimation of the global distribution of vertical velocity within cirrus clouds, Scientific Reports, 7(1), 6840, doi:https://doi.org/10.1038/s41598-017-07038-6.

Barahona, D., and A. Nenes (2011), Dynamical states of low temperature cirrus, Atmos. Chem. Phys., 11(8), 3757-3771, doi:https://doi.org/10.5194/acp-11-3757-2011.

Ceppi, P., F. Brient, M. D. Zelinka, and D. L. Hartmann (2017), Cloud feedback mechanisms and their representation in global climate models, WIREs Climate Change, 8(4), e465, doi:https://doi.org/10.1002/wcc.465.

Danabasoglu, G., et al. (2020), The Community Earth System Model Version 2 (CESM2), Journal of Advances in Modeling Earth Systems, 12(2), e2019MS001916, doi:https://doi.org/10.1029/2019MS001916.

Dean, S. M., J. Flowerdew, B. N. Lawrence, and S. D. Eckermann (2007), Parameterisation of orographic cloud dynamics in a GCM, Climate Dynamics, 28(6), 581-597, doi:https://doi.org/10.1007/s00382-006-0202-0.

Dean, S. M., B. N. Lawrence, R. G. Grainger, and D. N. Heuff (2005), Orographic cloud in a GCM: the missing cirrus, Climate Dynamics, 24(7), 771-780, doi:https://doi.org/10.1007/s00382-005-0020-9.

Delanoë, J., and R. J. Hogan (2010), Combined CloudSat-CALIPSO-MODIS retrievals of the properties of ice clouds, Journal of Geophysical Research: Atmospheres, 115(D4), doi:https://doi.org/10.1029/2009JD012346.

DeMott, P. J., D. J. Cziczo, A. J. Prenni, D. M. Murphy, S. M. Kreidenweis, D. S. Thomson, R. Borys, and D. C. Rogers (2003), Measurements of the concentration and composition of nuclei for cirrus formation, Proceedings of the National Academy of Sciences, 100(25), 14655-14660, doi:https://doi.org/10.1073/pnas.2532677100.

Dinh, T., A. Podglajen, A. Hertzog, B. Legras, and R. Plougonven (2016), Effect of gravity wave temperature fluctuations on homogeneous ice nucleation in the tropical tropopause layer, Atmos. Chem. Phys., 16(1), 35-46, doi:https://doi.org/10.5194/acp-16-35-2016.

Eidhammer, T., H. Morrison, A. Bansemer, A. Gettelman, and A. Heymsfield (2014), Comparison of ice cloud properties simulated by the Community Atmosphere Model (CAM5) with in-situ observations, Atmospheric Chemistry & Physics, 14(18), doi:https://doi.org/10.5194/acp-14-10103-2014.

Fritts, D. C., and M. J. Alexander (2003), Gravity wave dynamics and effects in the middle atmosphere, Reviews of Geophysics, 41(1), doi:https://doi.org/10.1029/2001RG000106.

Geller, M. A., et al. (2013), A Comparison between Gravity Wave Momentum Fluxes in Observations and Climate Models, Journal of Climate, 26(17), 6383-6405, doi:https://doi.org/10.1175/jcli-d-12-00545.1.

Gettelman, A., X. Liu, S. J. Ghan, H. Morrison, S. Park, A. J. Conley, S. A. Klein, J. Boyle, D. L. Mitchell, and J.-L. F. Li (2010), Global simulations of ice nucleation

and ice supersaturation with an improved cloud scheme in the Community Atmosphere Model, Journal of Geophysical Research: Atmospheres, 115(D18), doi:https://doi.org/10.1029/2009JD013797.
Gettelman, A., et al. (2019), The Whole Atmosphere Community Climate Model Version 6 (WACCM6), Journal of Geophysical Research: Atmospheres, 124(23), 12380-12403, doi:https://doi.org/10.1029/2019JD030943.
Gettelman, A., and H. Morrison (2015), Advanced Two-Moment Bulk Microphysics for Global Models. Part I: Off-Line Tests and Comparison with Other Schemes, Journal of Climate, 28(3), 1268-1287, doi:https://doi.org/10.1175/jcli-d-14-00102.1.
Golaz, J.-C., V. E. Larson, and W. R. Cotton (2002a), A PDF-Based Model for Boundary Layer Clouds. Part I: Method and Model Description, Journal of the Atmospheric Sciences, 59(24), 3540-3551, doi:https://doi.org/10.1175/1520-0469.
Golaz, J.-C., V. E. Larson, and W. R. Cotton (2002b), A PDF-Based Model for Boundary Layer Clouds. Part II: Model Results, Journal of the Atmospheric Sciences, 59(24), 3552-3571, doi:https://doi.org/10.1175/1520-0469.
Gregory, D., G. J. Shutts, and J. R. Mitchell (1998), A new gravity-wave-drag scheme incorporating anisotropic orography and low-level wave breaking: Impact upon the climate of the UK Meteorological Office Unified Model, Quarterly Journal of the Royal Meteorological Society, 124(546), 463-493, doi:https://doi.org/10.1002/qj.49712454606.
Haag, W., and B. Kärcher (2004), The impact of aerosols and gravity waves on cirrus clouds at midlatitudes, Journal of Geophysical Research: Atmospheres, 109(D12), doi:https://doi.org/10.1029/2004JD004579.
Hoose, C., and O. Möhler (2012), Heterogeneous ice nucleation on atmospheric aerosols: a review of results from laboratory experiments, Atmos. Chem. Phys., 12(20), 9817-9854, doi:10.5194/acp-12-9817-2012.
Hoyle, C. R., B. P. Luo, and T. Peter (2005), The Origin of High Ice Crystal Number Densities in Cirrus Clouds, Journal of the Atmospheric Sciences, 62(7), 2568-2579, doi:https://doi.org/10.1175/jas3487.1.
Jensen, E. J., and L. Pfister (2004), Transport and freeze-drying in the tropical tropopause layer, Journal of Geophysical Research: Atmospheres, 109(D2), doi:https://doi.org/10.1029/2003JD004022.
Jensen, E. J., L. Pfister, T. P. Bui, P. Lawson, and D. Baumgardner (2010), Ice nucleation and cloud microphysical properties in tropical tropopause layer cirrus, Atmos. Chem. Phys., 10(3), 1369-1384, doi:https://doi.org/10.5194/acp-10-1369-2010.
Jensen, E. J., et al. (1998), Ice nucleation processes in upper tropospheric wave-clouds observed during SUCCESS, Geophysical Research Letters, 25(9), 1363-1366, doi:https://doi.org/10.1029/98GL00299.
Joos, H., P. Spichtinger, and U. Lohmann (2009), Orographic cirrus in a future climate, Atmos. Chem. Phys., 9(20), 7825-7845, doi:https://doi.org/10.5194/acp-9-7825-2009.
Joos, H., P. Spichtinger, U. Lohmann, J.-F. Gayet, and A. Minikin (2008), Orographic cirrus in the global climate model ECHAM5, Journal of Geophysical Research: Atmospheres, 113(D18), doi:https://doi.org/10.1029/2007JD009605.

Kärcher, B., E. J. Jensen, and U. Lohmann (2019), The Impact of Mesoscale Gravity Waves on Homogeneous Ice Nucleation in Cirrus Clouds, Geophysical Research Letters, 46(10), 5556-5565, doi:https://doi.org/10.1029/2019GL082437.

Kärcher, B., and U. Lohmann (2002), A parameterization of cirrus cloud formation: Homogeneous freezing of supercooled aerosols, Journal of Geophysical Research: Atmospheres, 107(D2), AAC 4-1-AAC 4-10, doi:https://doi.org/10.1029/2001JD000470.

Kärcher, B., and J. Ström (2003), The roles of dynamical variability and aerosols in cirrus cloud formation, Atmos. Chem. Phys., 3(3), 823-838, doi:https://doi.org/10.5194/acp-3-823-2003.

Kim, Y. J., S. D. Eckermann, and H. Y. Chun (2003), An overview of the past, present and future of gravity‐wave drag parametrization for numerical climate and weather prediction models, Atmosphere-Ocean, 41(1), 65-98, doi:https://doi.org/10.3137/ao.410105.

Koop, T., B. Luo, A. Tsias, and T. Peter (2000), Water activity as the determinant for homogeneous ice nucleation in aqueous solutions, Nature, 406(6796), 611-614, doi:https://doi.org/10.1038/35020537.

Krämer, M., et al. (2016), A microphysics guide to cirrus clouds – Part 1: Cirrus types, Atmos. Chem. Phys., 16(5), 3463-3483, doi:https://doi.org/10.5194/acp-16-3463-2016.

Krämer, M., et al. (2020), A microphysics guide to cirrus – Part 2: Climatologies of clouds and humidity from observations, Atmos. Chem. Phys., 20(21), 12569-12608, doi:https://doi.org/10.5194/acp-20-12569-2020.

Lawson, R. P. (2011), Effects of ice particles shattering on the 2D-S probe, Atmos. Meas. Tech., 4(7), 1361-1381, doi:https://doi.org/10.5194/amt-4-1361-2011.

Lenschow, D. H. (1972), The measurement of air velocity and temperature using the NCAR Buffalo Aircraft Measuring System, Tech. Rep., Natl. Cent. for Atmos. Res., Boulder, Colo.

Lindzen, R. S. (1981), Turbulence and stress owing to gravity wave and tidal breakdown, Journal of Geophysical Research: Oceans, 86(C10), 9707-9714, doi:https://doi.org/10.1029/JC086iC10p09707.

Liou, K.-N. (1986), Influence of Cirrus Clouds on Weather and Climate Processes: A Global Perspective, Monthly Weather Review, 114(6), 1167-1199, doi:10.1175/1520-0493(1986)114<1167:Ioccow>2.0.Co;2.

Liu, X. (2000), Heterogeneous nucleation or homogeneous nucleation?, The Journal of Chemical Physics, 112(22), 9949-9955.

Liu, X., et al. (2012), Toward a minimal representation of aerosols in climate models: description and evaluation in the Community Atmosphere Model CAM5, Geosci. Model Dev., 5(3), 709-739, doi:https://doi.org/10.5194/gmd-5-709-2012.

Liu, X., P. L. Ma, H. Wang, S. Tilmes, B. Singh, R. C. Easter, S. J. Ghan, and P. J. Rasch (2016), Description and evaluation of a new four-mode version of the Modal Aerosol Module (MAM4) within version 5.3 of the Community Atmosphere Model, Geosci. Model Dev., 9(2), 505-522, doi:https://doi.org/10.5194/gmd-9-505-2016.

Liu, X., and J. Penner (2005), Ice nucleation parameterization for global models, Meteorologische Zeitschrift, 14, 499-514, doi:https://doi.org/10.1127/0941-2948/2005/0059.

Liu, X., J. E. Penner, S. J. Ghan, and M. Wang (2007), Inclusion of ice microphysics in the NCAR Community Atmospheric Model version 3 (CAM3), Journal of Climate, 20(18), 4526-4547, doi:https://doi.org/10.1175/JCLI4264.1.

Loeb, N., B. Wielicki, D. Doelling, G. Smith, and D. Keyes (2009), Toward optimal closure of the earth's top-of-atmosphere radiation budget, J. Clim., 22(3), 748–766, doi:10.1175/2008JCLI2637.1.

Lott, F., and M. J. Miller (1997), A new subgrid-scale orographic drag parametrization: Its formulation and testing, Quarterly Journal of the Royal Meteorological Society, 123(537), 101-127, doi:https://doi.org/10.1002/qj.49712353704.

Iacono, M. J., Delamere, J. S., Mlawer, E. J., Shephard, M. W., Clough, S. A., and Collins, W. D. (2008). Radiative forcing by long-lived greenhouse gases: Calculations with the AER radiative transfer models. Journal of Geophysical Research: Atmospheres, 113(D13). https://agupubs.onlinelibrary.wiley.com/doi/abs/10.1029/2008JD009944

Mace, G. G., E. E. Clothiaux, and T. P. Ackerman (2001), The Composite Characteristics of Cirrus Clouds: Bulk Properties Revealed by One Year of Continuous Cloud Radar Data, Journal of Climate, 14(10), 2185-2203, doi:https://doi.org/10.1175/1520-0442(2001)014<2185:Tccocc>2.0.Co;2.

McFarlane, N. A. (1987), The Effect of Orographically Excited Gravity Wave Drag on the General Circulation of the Lower Stratosphere and Troposphere, Journal of the Atmospheric Sciences, 44(14), 1775-1800, doi:https://doi.org/10.1175/1520-0469(1987)044<1775:Teooeg>2.0.Co;2.

Mitchell, D. L., A. Garnier, J. Pelon, and E. Erfani (2018), CALIPSO (IIR–CALIOP) retrievals of cirrus cloud ice-particle concentrations, Atmos. Chem. Phys., 18(23), 17325-17354, doi:https://doi.org/10.5194/acp-18-17325-2018.

Muhlbauer, A., T. P. Ackerman, J. M. Comstock, G. S. Diskin, S. M. Evans, R. P. Lawson, and R. T. Marchand (2014a), Impact of large-scale dynamics on the microphysical properties of midlatitude cirrus, Journal of Geophysical Research: Atmospheres, 119(7), 3976-3996, doi:https://doi.org/10.1002/2013JD020035.

Muhlbauer, A., H. Kalesse, and P. Kollias (2014b), Vertical velocities and turbulence in midlatitude anvil cirrus: A comparison between in situ aircraft measurements and ground-based Doppler cloud radar retrievals, Geophysical Research Letters, 41(22), 7814-7821, doi:https://doi.org/10.1002/2014GL062279.

Murphy, D. M. (2014), Rare temperature histories and cirrus ice number density in a parcel and a one-dimensional model, Atmos. Chem. Phys., 14(23), 13013-13022, doi:https://doi.org/10.5194/acp-14-13013-2014.

Murray, B. J., D. O'Sullivan, J. D. Atkinson, and M. E. Webb (2012), Ice nucleation by particles immersed in supercooled cloud droplets, Chemical Society Reviews, 41(19), 6519-6554, doi:10.1039/C2CS35200A.

Patnaude, R., Diao, M., Liu, X., and Chu, S.: Effects of thermodynamics, dynamics and aerosols on cirrus clouds based on in situ observations and NCAR CAM6, Atmos. Chem. Phys., 21, 1835-1859, 10.5194/acp-21-1835-2021, 2021.

Penner, J. E., C. Zhou, A. Garnier, and D. L. Mitchell (2018), Anthropogenic Aerosol Indirect Effects in Cirrus Clouds, Journal of Geophysical Research: Atmospheres, 123(20), 11,652-611,677, doi:https://doi.org/10.1029/2018jd029204.

Plougonven, R., and F. Zhang (2014), Internal gravity waves from atmospheric jets and fronts, Reviews of Geophysics, 52(1), 33-76, doi:https://doi.org/10.1002/2012RG000419.

Prasad, A. A., S. C. Sherwood, M. J. Reeder, and T. P. Lane (2019), Rapidly Evolving Cirrus Clouds Modulated by Convectively Generated Gravity Waves, Journal of Geophysical Research: Atmospheres, 124(13), 7327-7338, doi:https://doi.org/10.1029/2019JD030538.

Preusse, P., M. Ern, P. Bechtold, S. D. Eckermann, S. Kalisch, Q. T. Trinh, and M. Riese (2014), Characteristics of gravity waves resolved by ECMWF, Atmos. Chem. Phys., 14(19), 10483-10508, doi:https://doi.org/10.5194/acp-14-10483-2014.

Quante M., and D. O' C. Starr (2002), Dynamic processes in cirrus clouds: A review of observational results, in Cirrus, edited by D. K. Lynch, pp. 346–374, Oxford Univ. Press, New York, doi:https://doi.org/10.1093/oso/9780195130720.003.0021.

Richter, J. H., F. Sassi, and R. R. Garcia (2010), Toward a Physically Based Gravity Wave Source Parameterization in a General Circulation Model, Journal of the Atmospheric Sciences, 67(1), 136-156, doi:https://doi.org/10.1175/2009jas3112.1.

Scinocca, J. F., and N. A. McFarlane (2000), The parametrization of drag induced by stratified flow over anisotropic orography, Quarterly Journal of the Royal Meteorological Society, 126(568), 2353-2393, doi:https://doi.org/10.1002/qj.49712656802.

Shan, Y., X. Liu, L. Lin, Z. Ke, and Z. Lu (2021), An Improved Representation of Aerosol Wet Removal by Deep Convection and Impacts on Simulated Aerosol Vertical Profiles, Journal of Geophysical Research: Atmospheres, 126(13), e2020JD034173, doi:https://doi.org/10.1029/2020JD034173.

Shi, X., X. Liu, and K. Zhang (2015), Effects of pre-existing ice crystals on cirrus clouds and comparison between different ice nucleation parameterizations with the Community Atmosphere Model (CAM5), Atmos. Chem. Phys., 15(3), 1503-1520, doi:10.5194/acp-15-1503-2015.

Shi, X., and X. Liu (2016), Effect of cloud-scale vertical velocity on the contribution of homogeneous nucleation to cirrus formation and radiative forcing, Geophysical Research Letters, 43(12), 6588-6595, doi:https://doi.org/10.1002/2016GL069531.

Shi, X., S. Zhu, X. Zhi, K. Du, Q. Liu, and L. Wang (2017), Sensitive study on three ice nucleation parameterizations, Transactions of Atmospheric Sciences, 40, 181-192, doi:https://doi.org/10.13878/j.cnki.dqkxxb.20160914001.

Shi, Y., and X. Liu (2019), Dust Radiative Effects on Climate by Glaciating Mixed-Phase Clouds, Geophysical Research Letters, 46(11), 6128-6137, doi:https://doi.org/10.1029/2019GL082504.

Sourdeval, O., E. Gryspeerdt, M. Krämer, T. Goren, J. Delanoë, A. Afchine, F. Hemmer, and J. Quaas (2018), Ice crystal number concentration estimates from lidar–radar satellite remote sensing – Part 1: Method and evaluation, Atmos. Chem. Phys., 18(19), 14327-14350, doi:https://doi.org/10.5194/acp-18-14327-2018.

Stephens, G. L. (2005), Cloud Feedbacks in the Climate System: A Critical Review, Journal of Climate, 18(2), 237-273, doi:https://doi.org/10.1175/jcli-3243.1.
Teixeira, M. A. C. (2014), The physics of orographic gravity wave drag, Frontiers in Physics, 2, doi:10.3389/fphy.2014.00043.
Wang, Y., X. Liu, C. Hoose, and B. Wang (2014), Different contact angle distributions for heterogeneous ice nucleation in the Community Atmospheric Model version 5, Atmos. Chem. Phys., 14(19), 10411-10430, doi:10.5194/acp-14-10411-2014.
Wetherald, R., and S. Manabe (1988), Cloud Feedback Processes in a General Circulation Model, Journal of the Atmospheric Sciences, 45, 1397-1415, doi:https://doi.org/10.1175/1520-0469(1988)045<1397:CFPIAG>2.0.CO;2.
Wu, M., et al. (2020), Understanding processes that control dust spatial distributions with global climate models and satellite observations, Atmos. Chem. Phys., 20(22), 13835-13855, doi:https://doi.org/10.5194/acp-20-13835-2020.
Yu, P., et al. (2019), Efficient In-Cloud Removal of Aerosols by Deep Convection, Geophysical Research Letters, 46(2), 1061-1069, doi:https://doi.org/10.1029/2018GL080544.
Zhang, G. J., and McFarlane, N. A. (1995). Sensitivity of climate simulations to the parameterization of cumulus convection in the Canadian climate centre general circulation model. Atmosphere-Ocean, 33(3), 407-446. https://doi.org/10.1080/07055900.1995.9649539
Zhang, K., X. Liu, M. Wang, J. M. Comstock, D. L. Mitchell, S. Mishra, and G. G. Mace (2013), Evaluating and constraining ice cloud parameterizations in CAM5 using aircraft measurements from the SPARTICUS campaign, Atmos. Chem. Phys., 13(9), 4963-4982, doi:https://doi.org/10.5194/acp-13-4963-2013.
Zhao, X., Lin, Y., Peng, Y., Wang, B., Morrison, H., and Gettelman, A. (2017), A single ice approach using varying ice particle properties in global climate model microphysics, J. Adv. Model. Earth Syst., 9, 2138– 2157, doi:10.1002/2017MS000952.

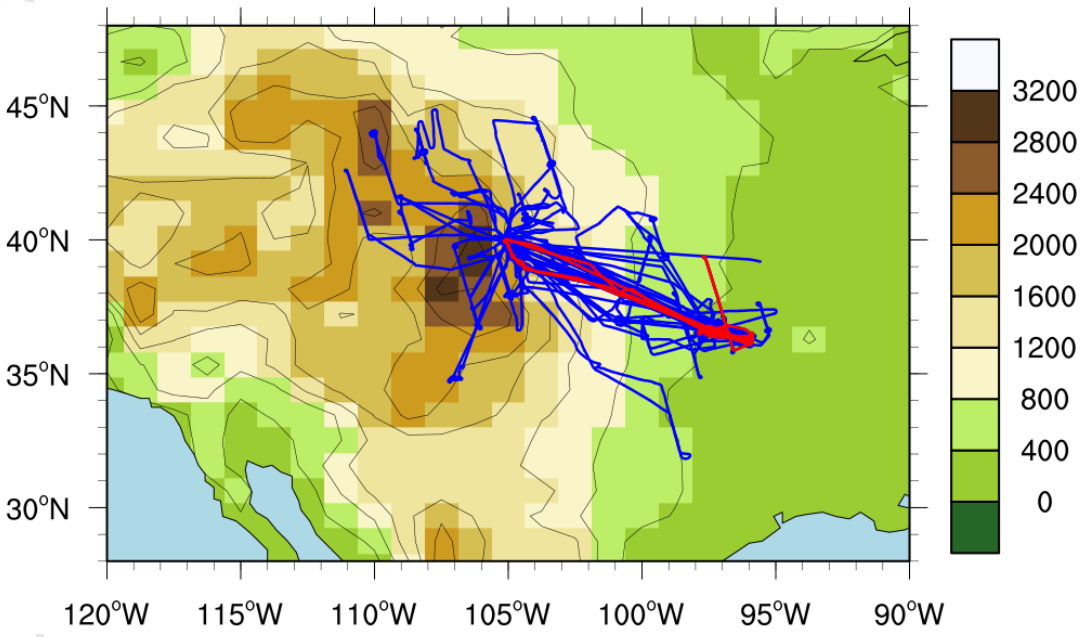

Figure 1. Aircraft trajectories (solid blue lines) during the SPARTICUS campaign. Color shading and black line contours show the surface terrain (unit: m). The solid red lines are flight tracks in the days (March 19, 30, April 1, 28, and 29, 2010) when ridge-crest cirrus was observed.

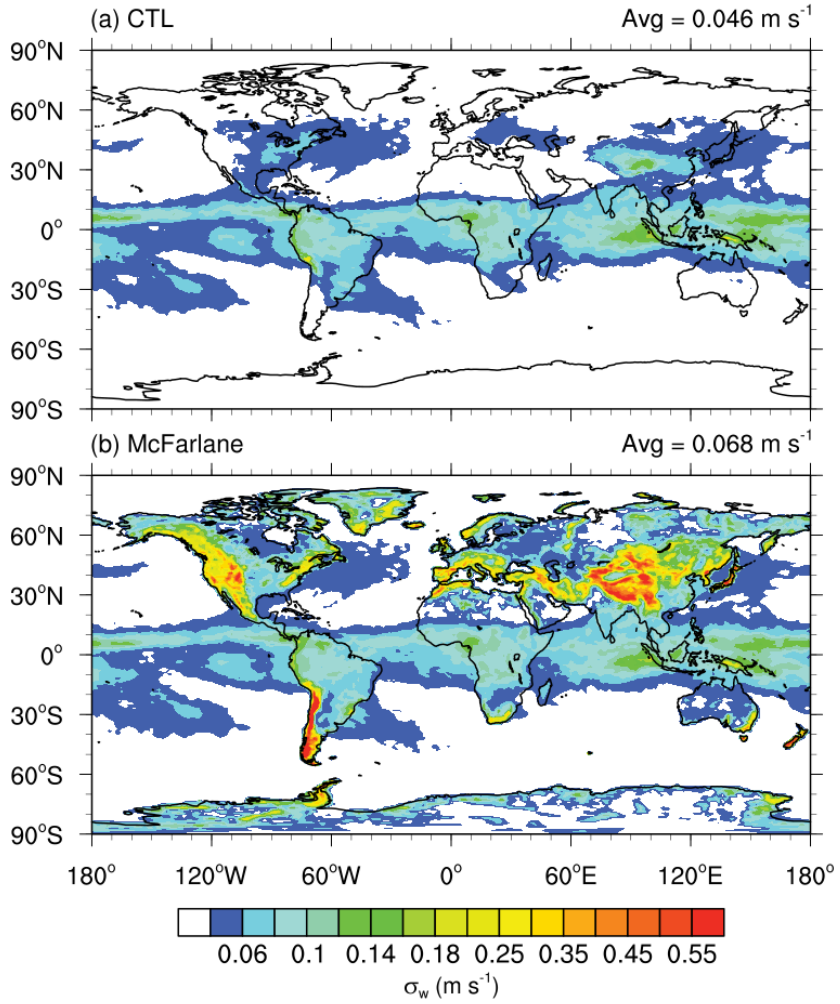

Figure 2. Global distribution of annual mean sub-grid scale vertical velocity variance (σ_w) for cirrus formation (m s^{-1}) from nudged simulations **(a)** CTL and **(b)** McFarlane during the SPARTICUS campaign in the upper troposphere (250 hPa). The value to the right of each title represents the global average weighted by the area.

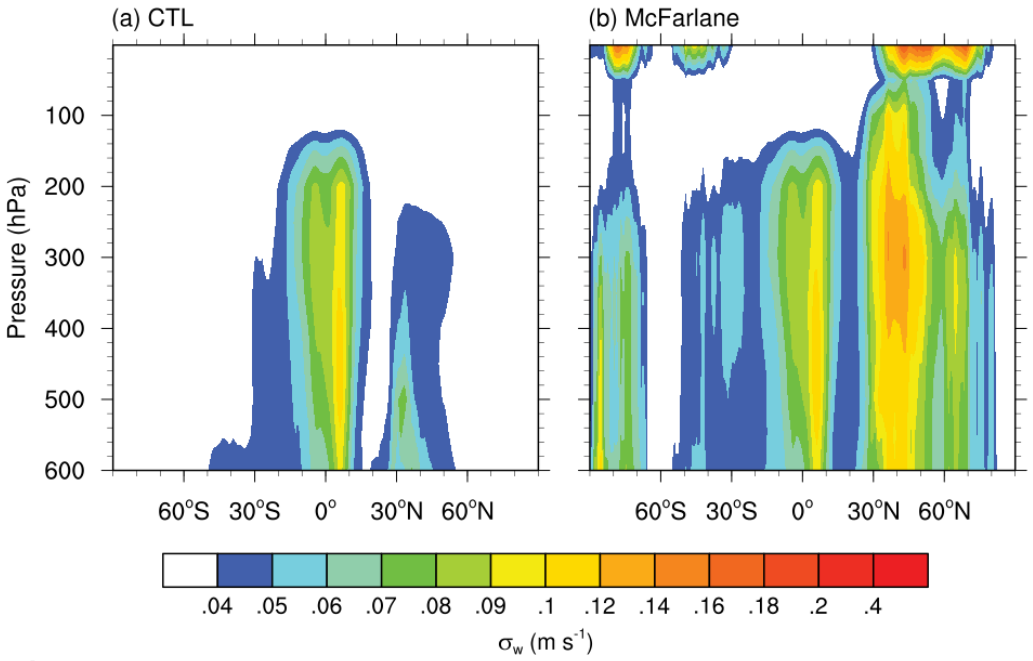

Figure 3. Annual zonal mean distribution of sub-grid scale σ_w for ice formation (m s^{-1}) from nudged simulations **(a)** CTL and **(b)** McFarlane during the SPARTICUS campaign in the upper troposphere (above 600 hPa).

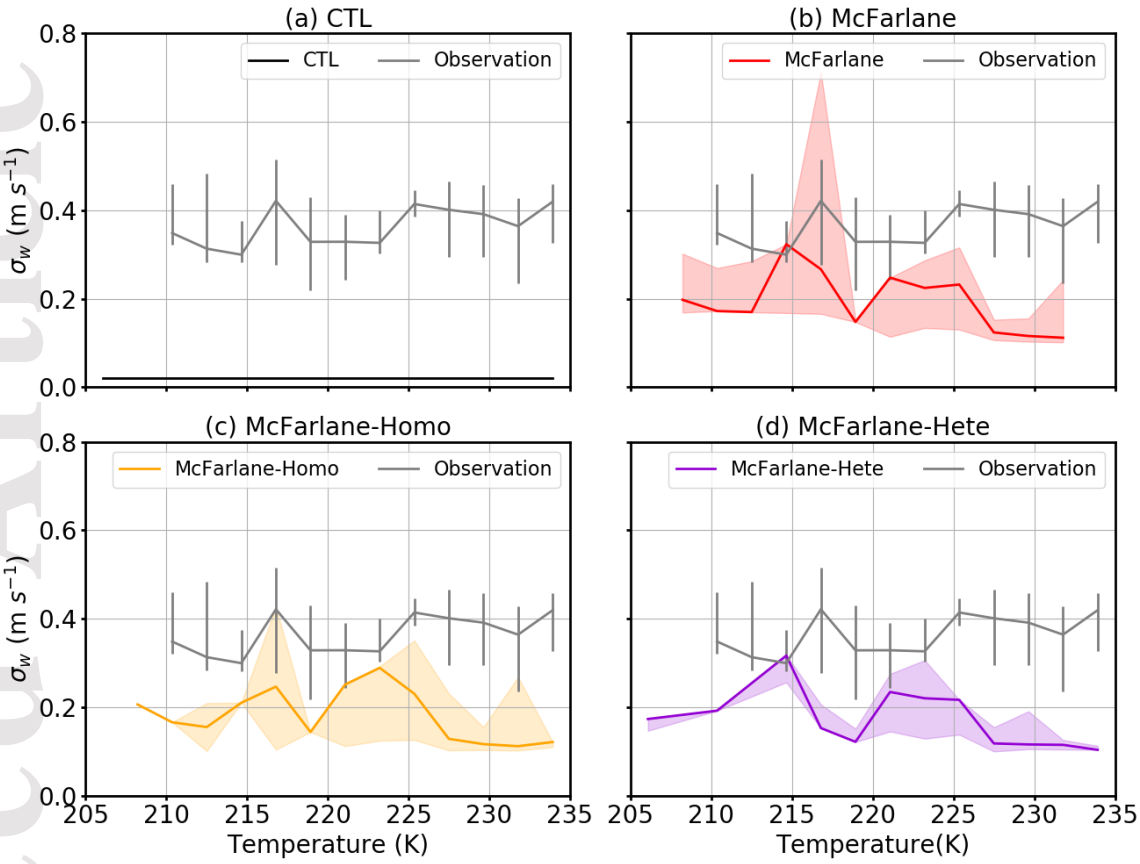

Figure 4. Variation of fast-speed σ_w ($\sigma_w \geq 0.1$ m s^{-1}) with temperature between observations and simulation results in ridge-crest cirrus during the SPARTICUS campaign. 0.1 m s^{-1} is the low limit when calculating σ_w in nudge simulations **(b)** McFarlane, **(d)** McFarlane-Hete, **(e)** McFarlane-Homo and **(a)** observations. Because most values in nudge **(c)** CTL simulation are smaller than 0.1 m s^{-1}, 0.1 m s^{-1} threshold is not used in this case. The solid lines are the median values. The shaded

areas are simulation results from the 25th percentile to the 75th percentile, and the bars are observations from the 25th percentile to the 75th percentile.

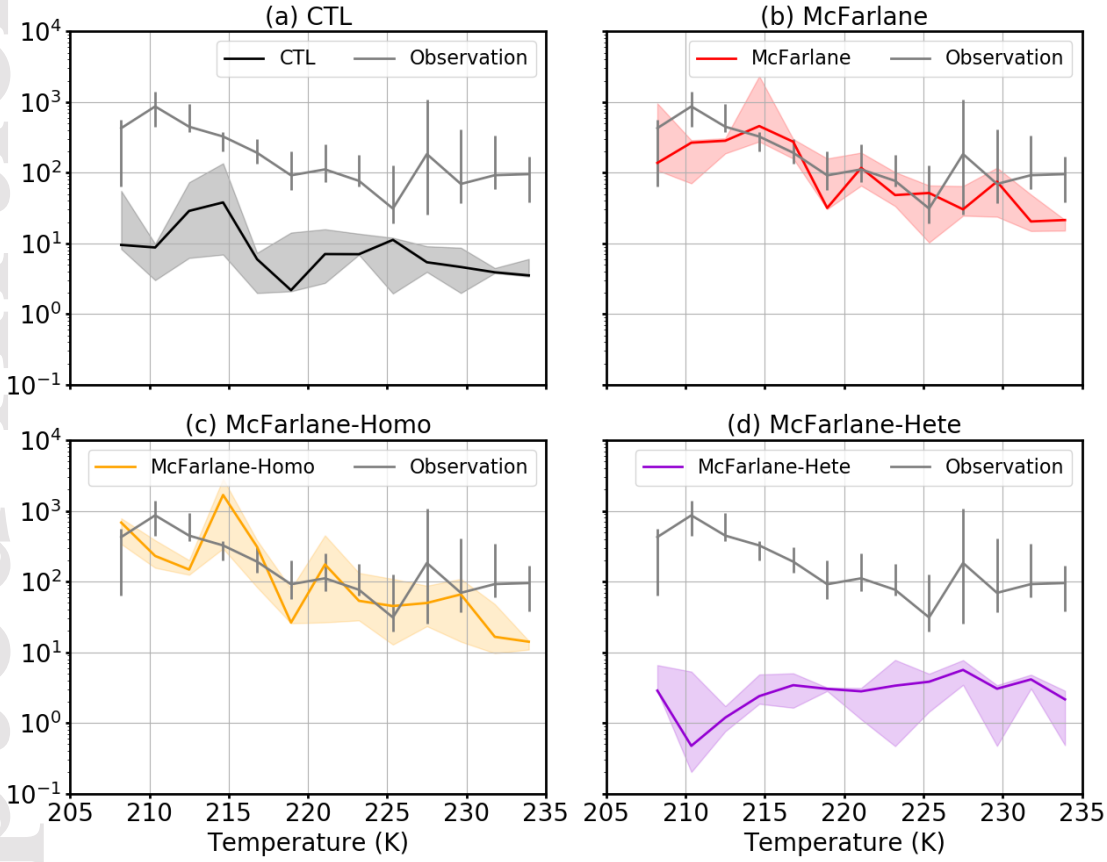

Figure 5. Variation of in-cloud ice number concentration (N_i) with temperature between observations and simulation results in ridge-crest cirrus during the SPARTICUS campaign. The solid lines are the median values. The shaded areas are simulation results from the 25th percentile to the 75th percentile, and the bars are observations from the 25th percentile to the 75th percentile.

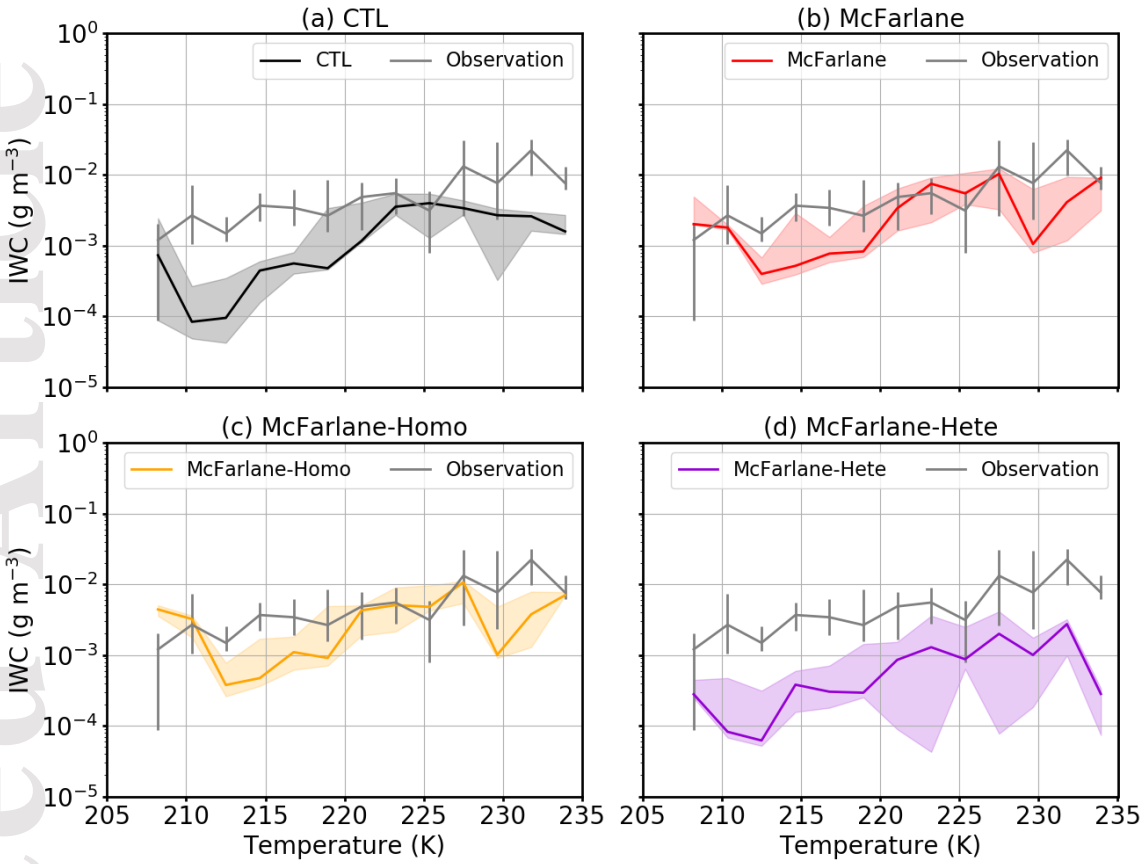

Figure 6. Variation of ice water content (IWC) with temperature between observations and simulation results in ridge-crest cirrus during the SPARTICUS campaign. The solid lines are the median values. The shaded areas are simulation results from the 25th percentile to the 75th percentile, and the bars are observations from the 25th percentile to the 75th percentile.

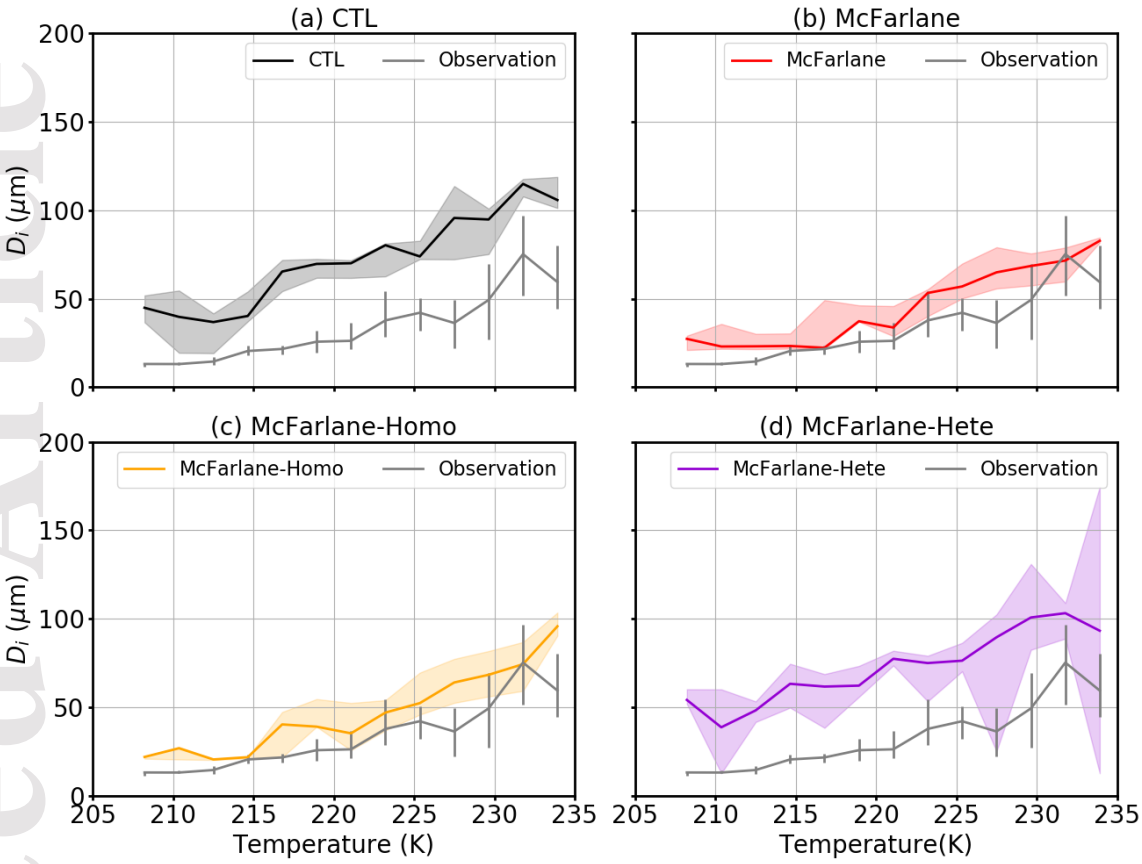

Figure 7. Variation of ice number weighted mean diameter (D_i) with temperature between observations and simulation results in ridge-crest cirrus during the SPARTICUS campaign. The solid lines are the median values. The shaded areas are simulation results from the 25th percentile to the 75th percentile, and the bars are observations from the 25th percentile to the 75th percentile.

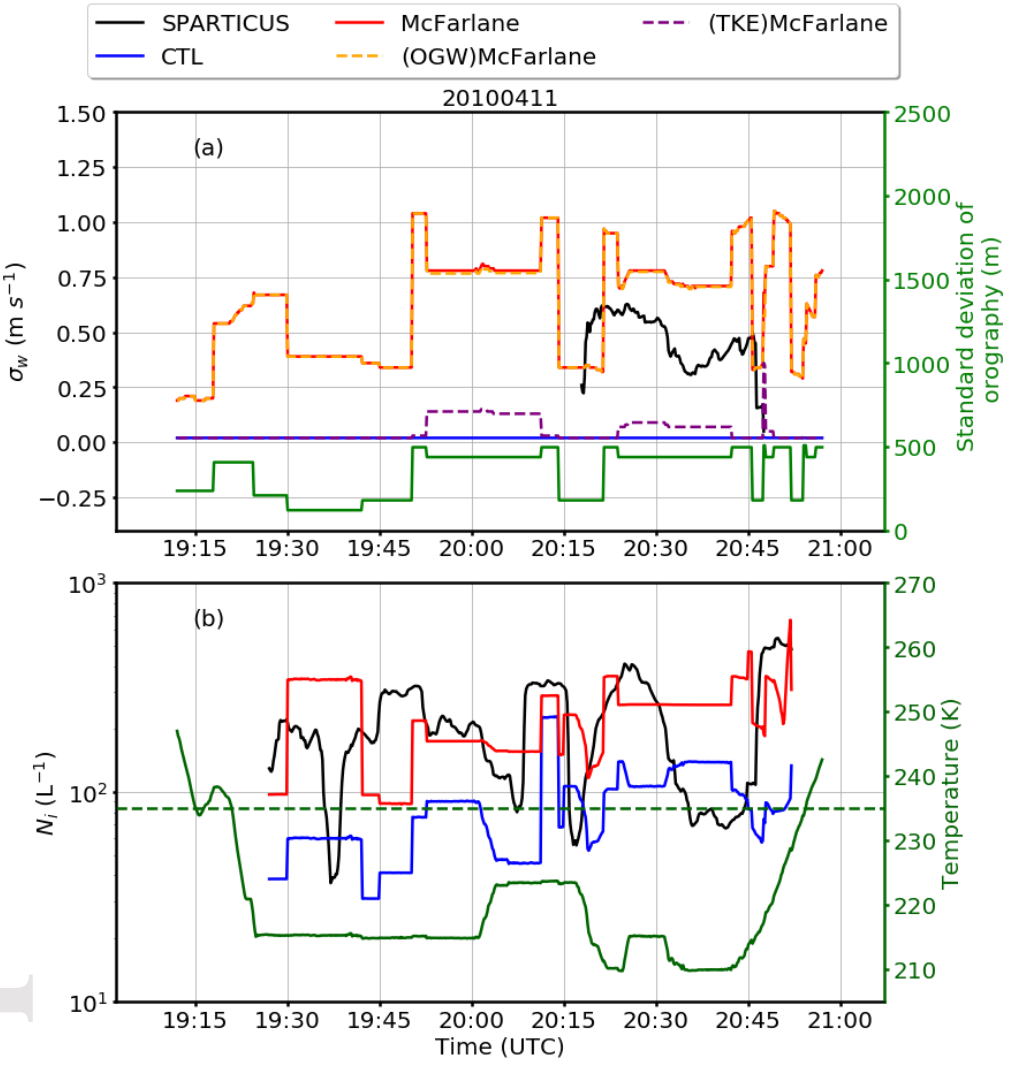

Figure 8. σ_w, N_i, and standard deviation of orography along the flight tracks on April 11. The black lines are from observation, the blue lines are from the CTL simulation, and the red lines are from the modified model with the McFarlane scheme OGW-induced σ_w. The orange lines in **(a)** are the OGW component of simulated σ_w, and the

pink lines are the CLUBB-TKE component of simulated σ_w. The green lines in **(a)** are the standard deviation of orography extracted from the model. The dark green solid lines in **(b)** are temperatures in the nudged McFarlane simulation. The dark green dashed lines in **(b)** are 235 K lines. The first and last 15 min of N_i during the flights are excluded to avoid bias due to the limitation of instruments when taking off and landing.

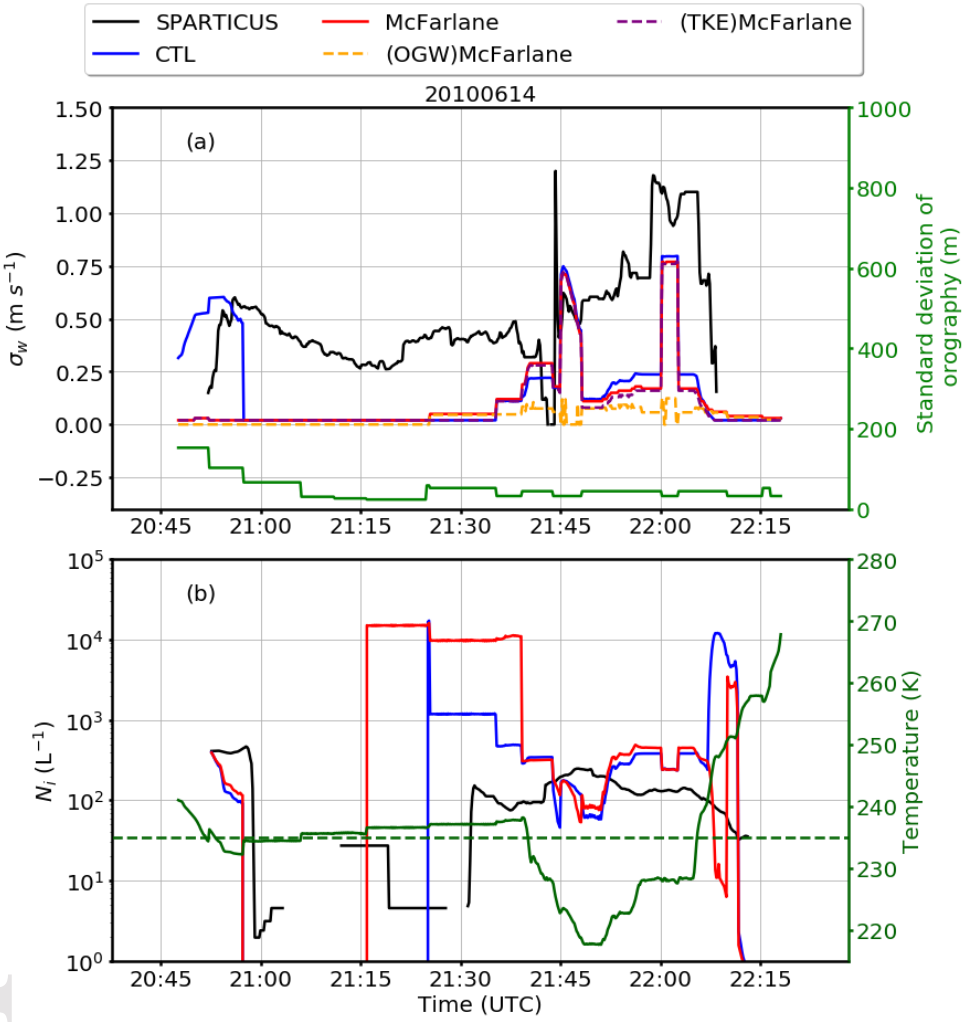

Figure 9. Similar to Fig. 8 but along the flight tracks on June 14, 2010.

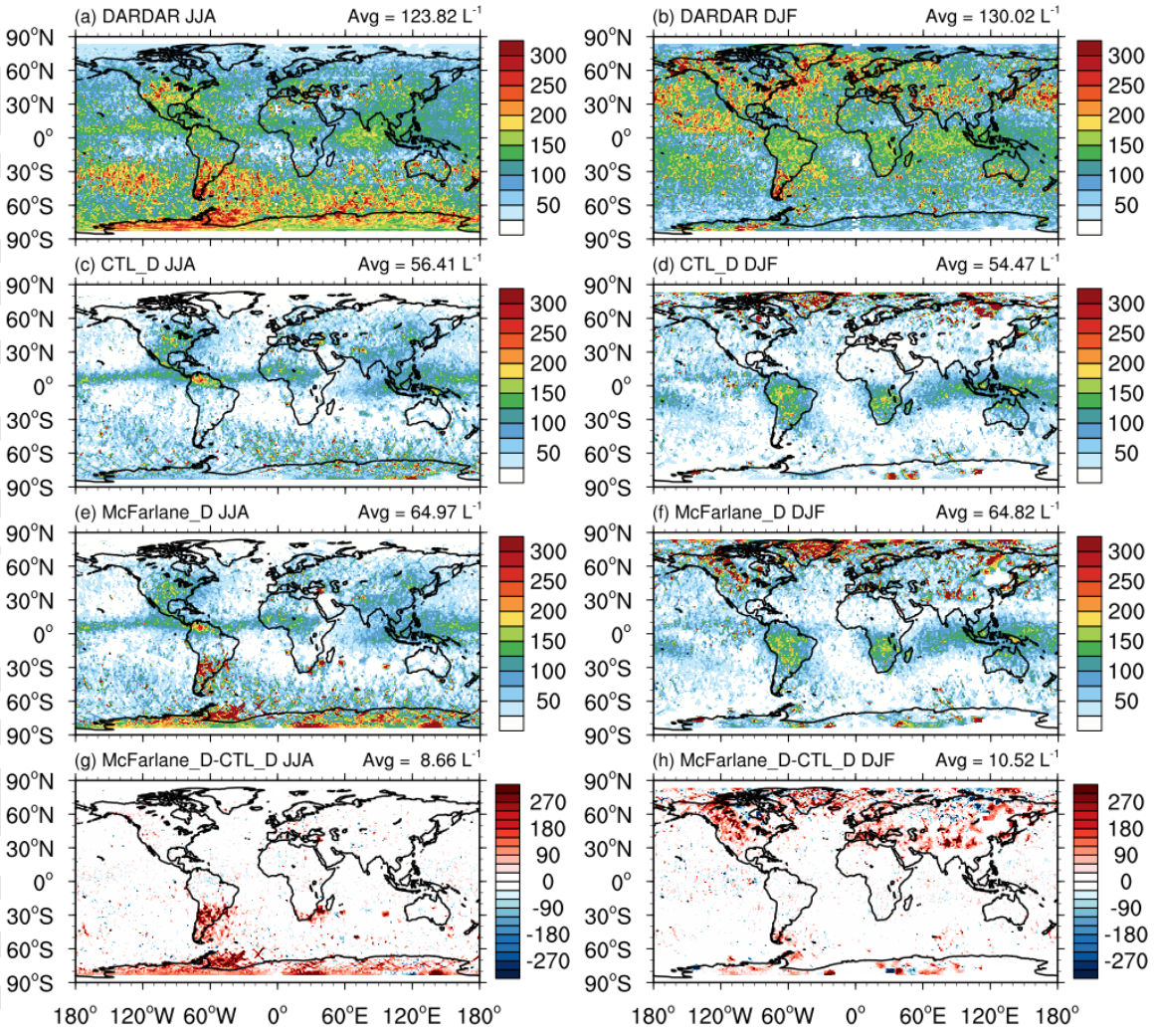

Figure 10. Seasonal global mean N_i at 226 hPa from DARDAR data and model simulations (CTL_D and McFarlane_D) from 2007 to 2009 along the CALIPSO satellite tracks. The N_i values are averaged over cloudy and clear-sky periods. Only N_i with diameters larger than 5 μm, IWC $\geq 1 \times 10^{-3}$ g kg^{-1} and grid ice cloud fraction

larger than 0.01 are considered. The value to the right of each title represents the global average weighted by the area.

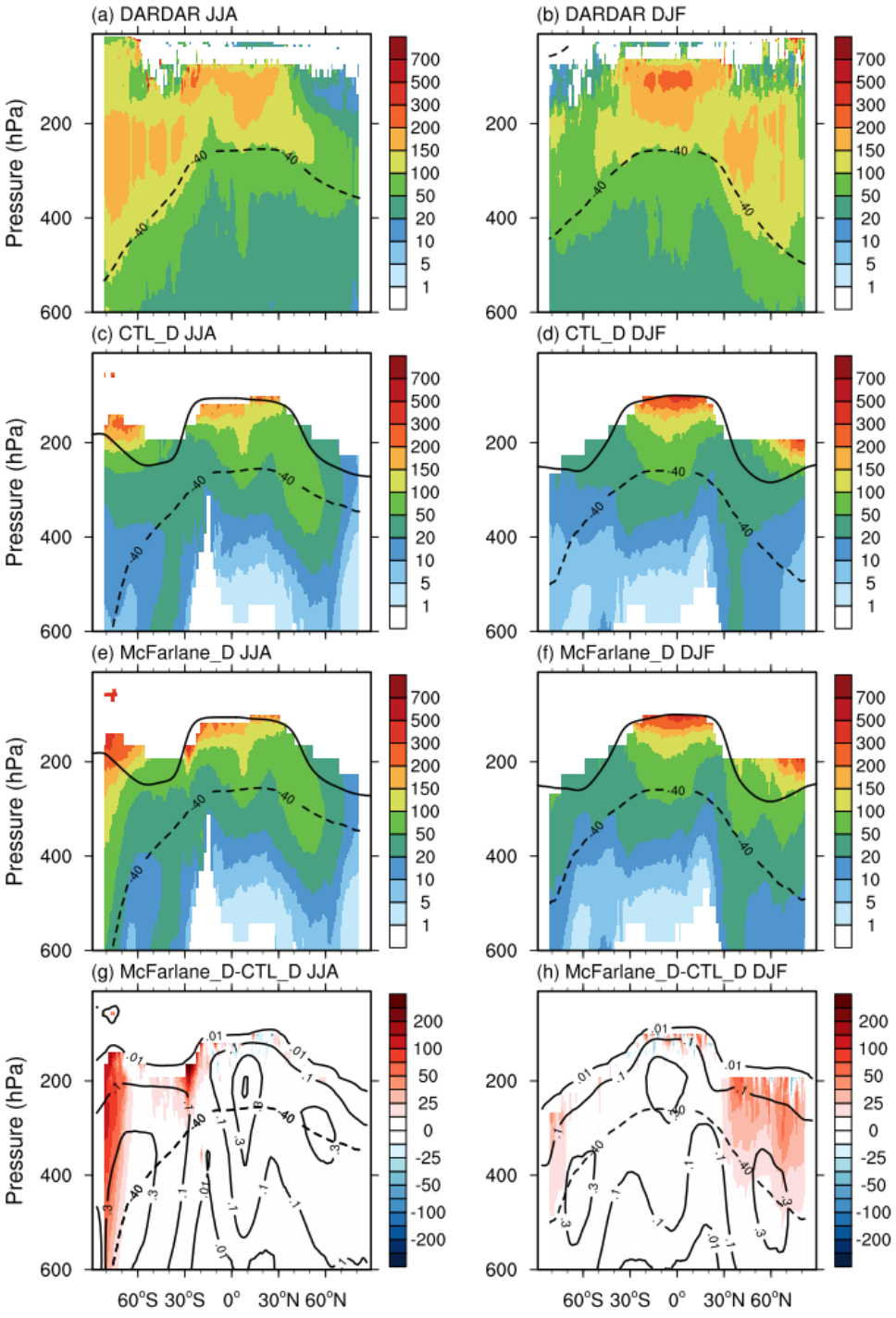

Figure 11. Seasonal zonal mean N_i between DARDAR and simulations (CTL_D and McFarlane_D) from 2007 to 2009 along the CALIPSO satellite tracks. The dashed line is the annual mean -40°C isothermal line. The solid lines in **(c)**, **(d)**, **(e)** and **(f)** are the tropopause in the simulations. The solid lines in **(g)** and **(h)** are ice cloud frequencies in the McFarlane_D simulation. The N_i values are averaged over cloudy and clear-sky periods. Only N_i with diameters larger than 5 μm, IWC $\geq 1 \times 10^{-3}$ g kg^{-1} and grid ice cloud fraction larger than 0.01 are considered.

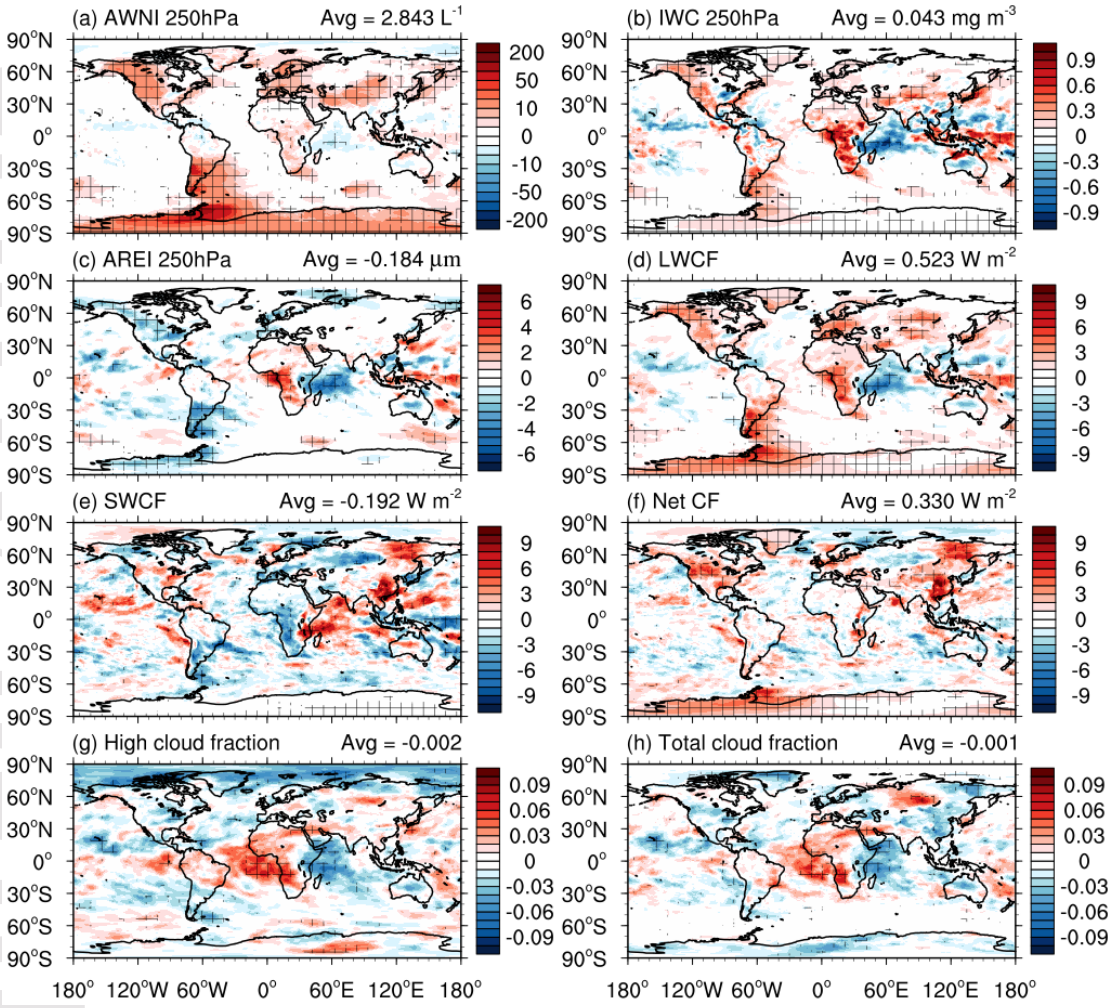

Figure 12. The annual mean difference of grid-averaged ice number concentration (AWNI) at 250 hPa, grid-averaged IWC at 250 hPa, grid-averaged ice effective radius (AREI) at 250 hPa, longwave cloud forcing (LWCF), shortwave cloud forcing (SWCF), net cloud forcing (net CF), high cloud fraction and total cloud fraction between the McFarlane-Climo simulation and the CTL-Climo simulation in 6-year

climatological simulations. Areas with meshed grids indicate the values with a statistical significance level passing 5%. The value to the right of each title represents the global average weighted by the area.

Table 1. *Description of Simulations*

Model experiment	Resolution	Period	Description
CTL	0.9º×1.25º, 56L	2009 January to 2010 June	Default CAM6, only consider CLUBB-TKE-induced vertical velocity variance. (nudged UV)
McFarlane	0.9º×1.25º, 56L	2009 January to 2010 June	Same as default CAM6 but also consider orographic gravity waves based on the McFarlane scheme for vertical velocity variance. (nudged UV)
McFarlane-Homo	0.9º×1.25º, 56L	2009 January to 2010 June	Same as McFarlane but consider only homogenous ice nucleation. (nudged UV)
McFarlane-Hete	0.9º×1.25º, 56L	2009 January to 2010 June	Same as McFarlane but consider only heterogenous ice nucleation. (nudged UV)

CTL_D	0.9º×1.25º, 56L	2006 October to 2009 December	Same as CTL except simulation period. (nudged UV)
McFarlane_D	0.9º×1.25º, 56L	2006 October to 2009 December	Same as McFarlane except simulation period. (nudged UV)
CTL-Climo	0.9º×1.25º, 56L	6-year climatology	Same as CTL except simulation period. (without nudged UV)
McFarlane-Climo	0.9º×1.25º, 56L	6-year climatology	Same as McFarlane except simulation period. (without nudged UV)

Table 2. *Range of Meteorological Conditions and Ice Microphysical Properties for Cirrus Clouds and Ridge-crest Cirrus in the SPARTICUS Observations and CAM6 Simulations*

	SPARTICUS	CTL	McFarlane	McFarlane-Homo	McFarlane-Hete
T [K]	207.81–233.13	206.20–233.14	205.34–233.15	205.30–233.15	204.64–233.15
N_i [L^{-1}]	0.20–2984.50	0.13–229.02	2.25–10109.60	2.70–3690.34	0.024–56.10
D_i [μm]	10.50–154.17	11.80–322.34	10.16–237.56	10.10–234.68	10.04–323.64
IWC [g m^{-3}]	1.24×10^{-5}–0.12	1.19×10^{-5}–0.019	6.66×10^{-5}–0.020	6.22×10^{-5}–0.019	1.04×10^{-5}–0.0072
Occurrence of cirrus	16445	19743	19179	19672	20443
Occurrence of ridge-crest cirrus	2713	2415	2553	2575	3022

Table 3. *The Number of Fast-speed σ_w ($\sigma_w \geq 0.1$ m s^{-1}) Occurrence in Cirrus Clouds and Ridge-crest Cirrus Along Flight Tracks During the SPARTICUS Campaign*

	SPARTICUS	CTL	McFarlane	McFarlane-Homo	McFarlane-Hete
Cirrus	6918	3828	6916	7172	6429
Ridge-crest cirrus	1884	2	931	778	765